JGR Earth Surface

RESEARCH ARTICLE
10.1029/2021JF006172

Key Points:

- We conducted novel laboratory experiments to test five existing models for the high-frequency seismic signals generated by granular flows
- The "thin-flow" model of Farin, Tsai, et al. (2019, https://doi.org/10.1002/esp.4677) was the most accurate and makes predictions consistent with empirical observations
- The ratio between the mean and fluctuating forces exerted by a granular flow varies greatly, determined by an inertial number of the flow

Supporting Information:

Supporting Information may be found in the online version of this article.

Correspondence to:

M. I. Arran,
arran@ipgp.fr

Citation:

Arran, M. I., Mangeney, A., De Rosny, J., Farin, M., Toussaint, R., & Roche, O. (2021). Laboratory landquakes: Insights from experiments into the high-frequency seismic signal generated by geophysical granular flows. *Journal of Geophysical Research: Earth Surface*, *126*, e2021JF006172. https://doi.org/10.1029/2021JF006172

Received 21 MAR 2021
Accepted 1 APR 2021

Laboratory Landquakes: Insights From Experiments Into the High-Frequency Seismic Signal Generated by Geophysical Granular Flows

M. I. Arran[1], A. Mangeney[1], J. De Rosny[2], M. Farin[2], R. Toussaint[3,4], and O. Roche[5]

[1]Institut de Physique du Globe de Paris, CNRS, Université de Paris, Paris, France, [2]Institut Langevin, ESPCI Paris, CNRS, PSL University, Paris, France, [3]Institut Terre et Environnement de Strasbourg, UMR 7063, CNRS, Université de Strasbourg, Strasbourg, France, [4]SFF PoreLab, Department of Physics, The Njord Centre, University of Oslo, Oslo, Norway, [5]Laboratoire Magmas et Volcans, CNRS, IRD, OPGC, Université Clermont Auvergne, Clermont-Ferrand, France

Abstract Geophysical granular flows exert basal forces that generate seismic signals, which can be used to better monitor and model these severe natural hazards. A number of empirical relations and existing models link these signals' high-frequency components to a variety of flow properties, many of which are inaccessible by other analyses. However, the range of validity of the empirical relations remains unclear and the models lack validation, owing to the difficulty of adequately controlling and instrumenting field-scale flows. Here, we present laboratory experiments investigating the normal forces exerted on a basal plate by dense and partially dense flows of spherical glass particles. We measured the power spectra of these forces and inferred predictions for these power spectra from the models for debris flows' seismic signals proposed by Kean et al. (2015, https://doi.org/10.1002/2015GL064811), Lai et al. (2018, https://doi.org/10.1029/2018GL077683), and Farin, Tsai, et al. (2019, https://doi.org/10.1002/esp.4677), using Hertz theory to extend Farin, Tsai, et al. (2019)'s models to higher frequencies. Comparison of our observations to these predictions, and to predictions derived from Bachelet (2018) and Bachelet et al. (2021)'s model for granular flows' seismic signals, shows those of Farin, Tsai, et al. (2019)'s "thin-flow" model to be the most accurate, so we examine explanations for this accuracy and discuss its implications for geophysical flows' seismic signals. We also consider the normalization, by the mean force exerted by each flow, of the force's mean squared fluctuations, showing that this ratio varies by 4 orders of magnitude over our experiments, but is determined by the bulk inertial number of the flow.

Plain Language Summary Landslides, like earthquakes, generate seismic signals: vibrations of the earth that can be detected a long way away. Analysis of the most rapid vibrations could provide information about how large a landslide is or how damaging it will be, helping emergency services respond. But full-size landslides are complex and difficult to study, so the generation of these vibrations is not yet sufficiently well understood for this information to be reliable. Therefore, in the place of full-size landslides, we studied simplified, small-scale versions in the laboratory, testing previous authors' predictions for the seismic signals they generate. We find that one set of predictions was particularly accurate and show that the corresponding predictions for full-size landslides are consistent with previous observations. This implies that a landslide's seismic signal can be used to calculate its size, its speed, and the typical size of particles within it.

1. Introduction

1.1. Background

Landslides and other geophysical granular flows are a major natural hazard, causing on average 4,000 deaths worldwide each year from 2004 to 2016 (Froude & Petley, 2018) and an estimated billions of dollars of annual damage in the United States alone (Fleming et al., 1980; National Research Council, 1985; Schuster & Fleming, 1986). Few areas have an early warning system in place (Guzzetti et al., 2020) and a damaging event's magnitude and effects may remain unknown for hours or days after it happens (Hervás, 2003; Scholl et al., 2017), hindering the response of emergency services. Modeling is currently unable to remedy these knowledge gaps or to accurately identify the hazardous areas that should be avoided, with poorly constrained parameters, such as a flow's basal friction coefficient, being important in determining a landslide's runout (Cuomo, 2020; Delannay et al., 2017; Lucas et al., 2014; van Asch et al., 2007).

Better monitoring of landslide-prone areas and better modeling of flows' evolution are therefore key to the reduction of landslide hazard, and the use of seismic signals is a promising tool toward these aims. Geophysical flows exert forces on the ground over which they travel, resulting in the outwards-propagating seismic waves that Kanamori and Given (1982) first described in detail, for a rock avalanche at Mount St. Helens. These seismic waves, which we refer to as "landquakes," can be detected by a local or regional seismic network, permitting continuous monitoring of a wide area. This monitoring suggests the possibility of early warning systems, analogous to those in use and development for earthquakes (e.g., Given et al., 2018). Furthermore, landquakes encode information about a landslide's magnitude and evolution over time, and so these seismic signals can be analyzed to assess damage, to constrain model parameters, and to compare different models.

However, the low-frequency components of landquakes studied by Kanamori and Given (1982) can typically only be detected for large landslides ($>10^7$ m^3 according to Allstadt et al. [2018]) and are predominantly generated by the accelerations of a landslide's center of mass (Dahlen, 1993; Fukao, 1995; Kawakatsu, 1989). Therefore, even when detected, they cannot provide information on many properties relevant to landslide modeling and harm assessment, such as the size of individual particles within the flow or the vertical profiles of flow properties.

To extract more information and infer these properties, previous authors suggest using the high-frequency component of landquakes, generated by the rapidly fluctuating forces exerted by the flow and associated with the accelerations of individual particles within it. The spectrogram of this high-frequency component and its envelope have distinctive shapes (Suriñach et al., 2005) which can be used to detect landslides (e.g., Dammeier et al., 2016; Fuchs et al., 2018; Hibert et al., 2014; Lee et al., 2019). Furthermore, the properties of this envelope can be related to those of the landslide: the envelope's duration to the landslide's duration and hence its loss of potential energy (Deparis et al., 2008; Hibert et al., 2011; Levy et al., 2015); the envelope's amplitude to the seismic energy emitted by the landslide and hence its volume (Hibert et al., 2011; Levy et al., 2015; Norris, 1994), its work rate against friction (Levy et al., 2015; Schneider et al., 2010), and its momentum (Hibert et al., 2015, 2017); and envelope scale and shape parameters to the landslide's geometry via multilinear regression (Dammeier et al., 2011). Some of these relations have been replicated in laboratory experiments on dry granular flows: Farin et al. (2018) links seismic envelopes' duration to potential energy loss and envelopes' shape to flows' varying vertical and horizontal momenta, for collapses of granular columns on angled planes, while Farin, Mangeney, et al. (2019) proposes an expression for a collapse's net seismic energy emission, in terms of the column's mass, aspect ratio, particle diameter, and maximum center of mass velocity.

Other laboratory experiments have investigated the dynamics by which granular flows generate high-frequency signals, in geometries including discharging silos (Gardel et al., 2009), rotating drums (Hsu et al., 2014), and rotary shear cells (Taylor & Brodsky, 2017). Gardel et al. (2009), calculating the power spectra of the forces that flows exert on their boundaries, shows the amplitude of high-frequency force fluctuations to increase with increasing flow rate. Hsu et al. (2014), meanwhile, shows the typical magnitude of such fluctuations to increase with increases in flow rate and grain size, with the mean force exerted over macroscopic flow timescales, and with the shear-determined "inertial stress" σ_i, as approximately $\sigma_i^{0.5}$ for flows of water-saturated gravel. This is broadly consistent with Taylor and Brodsky (2017)'s observation that, under constant mean pressure, granular flows' force fluctuations induced boundary vibrations with squared amplitude proportional to d^3I, for grain diameter d and estimate I of the "inertial number": a local, non-dimensional shear rate, with its square equal to the ratio between the inertial stress and the mean stress, that previous authors suggest will uniquely determine all other local, non-dimensional flow parameters (GDR; da Cruz et al., 2005; Jop et al., 2006; MiDi, 2004).

However, there are discrepancies between the relations suggested by different authors, including the difference between a landslide's momentum and its work against friction, and different exponents in power laws for force fluctuations' amplitude as a function of I. Furthermore, the relations are empirical, so both their precision and their range of validity are unclear. Allstadt et al. (2020)'s large-scale experiments, for example, identify no simple relations between the properties of debris flows and of the fluctuating forces they exert, despite excellent instrumentation. To reliably link landslides' properties to those of the high-frequency seismic signals they generate, a mechanistic model for landquake generation is required.

1.2. Existing Models

Models of the high-frequency component of landquakes rely on the same framework: consideration of the total seismic signal as a sum of the uncorrelated signals generated by individual, random particle impacts, with i) the properties of the impacts determined by some mean properties of the particulate flow and ii) a specified Green's function mapping the force of an individual impact to the seismic signal observed at a remote station. This stochastic impact framework arises from Tsai et al. (2012)'s model of seismic noise generation from riverine sediment transport, and Gimbert et al. (2019) validates it in that context using flume experiments. We discuss its validity for landquakes in Text S2, showing that it will be applicable to any extensive flows of stiff particles for which energetic impacts are more significant than other high-frequency sources, for signal periods smaller than the timescales over which the bulk flow varies. Examples may include avalanches, the coarse-grained fronts of debris flows, and rockfalls involving multiple blocks.

Assuming the framework's validity, prediction of a flow volume V's high-frequency landquake signal requires consideration of the locations $\mathbf{x} \in V$ of signal generation, and the specification of just three things at each location: 1) the number $n_I(\mathbf{x})$ of impacts per unit volume and time; 2) the force $\mathbf{F}_I(\mathbf{x}, t)$ applied by a single, typical impact over its duration; and 3) the Green's function $\mathbf{G}(t, \mathbf{r}; \mathbf{x})$ for each single-component velocity response $v_\mathbf{r}(t)$ to that force of the seismic station detecting the signal, located at $\mathbf{r}$. Writing $\tilde{\cdot}$ for Fourier transforms over time Δt, the landquake signal will then have power spectral density

$$P_{v_\mathbf{r}}(f) = \left|\tilde{v}_\mathbf{r}(f)\right|^2 / \Delta t = \int_V n_I(\mathbf{x}) \left|\tilde{\mathbf{F}}_I(\mathbf{x}, f) \cdot \tilde{\mathbf{G}}(f, \mathbf{r}; \mathbf{x})\right|^2 \mathrm{d}^3\mathbf{x}. \tag{1}$$

1.2.1. Direct Use of Tsai et al. (2012)

Kean et al. (2015), Lai et al. (2018), and Farin, Tsai, et al. (2019) consider only impacts at the base of a flow to be significant in signal generation, and assume 1) that the rate of impacts is determined by the advection of particles, with the mean flow, into basal irregularities of the same scale; 2) that the force a particle exerts varies over timescales much shorter than the range of periods to which the seismic station is sensitive; and 3) that the relevant Green's function is that for Rayleigh-wave propagation to the far field. Under these assumptions, if a representative impacting particle has diameter d and downslope speed u, it will have collision rate u/d, so that a bedrock-contacting flow area A in which impacting particles have a volume fraction ϕ will have an approximate integrated collision rate $\int_V n_I \,\mathrm{d}\mathbf{x} = \phi A u/d^3$. For all signal periods of interest, the typical force applied by an impact will be approximable as a Dirac delta function in time and hence constant in the frequency domain, equal to the impulse transferred, so that $\tilde{\mathbf{F}}_I(f) = \Delta p \mathbf{e}_I$ for a representative impulse magnitude Δp and unit vector $\mathbf{e}_I$. Meanwhile, the relevant frequency-space Green's function for a station at radius r will have magnitude $\left|\mathbf{e}_I \cdot \tilde{\mathbf{G}}\right| = R(f) e^{-\alpha(f) r} / \sqrt{r}$, for functions R and α related to Rayleigh-wave propagation and inelastic attenuation, respectively (Lamb, 1904). Consequently, the signal's power spectral density will be

$$P_{v_\mathbf{r}}(f) = \frac{\phi A u \Delta p^2}{d^3 r} R(f)^2 e^{-2\alpha(f) r}. \tag{2}$$

Material above the flow's base is supposed to affect the signal only via its influence on u and Δp.

Kean et al. (2015) suggests that u scales with the measured surface velocity and Δp with the mean stress exerted by the flow, equal to the base-normal component of the flow's local weight per unit area. The authors use an empirical, piecewise-continuous function α, and avoid consideration of scaling constants, ϕ, R, and d by examining only the ratio of $P_{v_\mathbf{r}}(f)$ to that measured during a reference debris flow in the same channel, for which such parameters are assumed to be the same. The paper uses this model to estimate the depths of static sediment "shielding" the channel center from impacts, and these estimates correctly remain positive, but the paper performs no further evaluation of the model.

Lai et al. (2018) suggests that large, flow-depth-spanning particles dominate the signal, so that d should be the 94th percentile of the particle diameter distribution and u should be the depth-averaged downslope velocity $\overline{u}$ of the flow. The authors implicitly take $\phi = 1$ and further assume that impacts transfer an impulse equal to that for elastic rebounds of individual near-spherical particles at vertical velocity $\overline{u}$, such that $\Delta p = \pi \rho d^3 \overline{u} / 3$ for particle material density ρ. Equations for $R(f)$ and $\alpha(f)$ are taken from Tsai et al. (2012), Tsai and Atiganyanun (2014), and Gimbert and Tsai (2015), and then applied to a Californian debris flow, to invert the peak frequency of $P_{v_{\mathbf{r}}}(f)$ for r. However, this inversion relies on the model for signal generation only via the assumption that $\left|\tilde{\mathbf{F}}_I(f)\right|$ is independent of f in the frequency range of interest, so this assumption is the only part of the model that the paper tests. Values for A, u, and d were inferred but not measured.

Farin, Tsai, et al. (2019) generalizes the model of Lai et al. (2018) to different flow regions and regimes and to a continuous particle size distribution. The authors calculate that the impacts of particles falling from the flow front or saltating ahead of it are less significant for signal generation than those in the flow's dense snout and body. In these two regions, for "thin" flows of depth h comparable to the largest particle diameters, the paper suggests that the Lai et al. (2018) model will hold, with slight modifications: ϕ is explicitly stated; there are extra terms in the equation for Δp to account for inelasticity and variation in the angle and velocity of impacts; R is adjusted to account for non-vertical $\mathbf{e}_I$; and d is represented by its appropriately weighted average over the distribution of particle diameters, which is suggested to be approximately equal to the 73rd percentile of that distribution. However, for "thick" flows, where h is much larger than the particles' diameters, the paper suggests that, in addition to the above slight modifications, the relevant advection and impact velocity is that of base-adjacent particles. Assuming no basal slip, in the sense that velocities tend to zero toward the flow's base, u is then proportional to $\overline{u} d / h$ and the representative value of d is equal to the 86th percentile of the particle diameter distribution. The authors tested neither of the "thin-flow" and "thick-flow" models.

1.2.2. Model of Bachelet et al.

In contrast to the above papers, Bachelet (2018) as well as of Bachelet et al. (2021) consider impacts between different layers of particles, throughout the depth of the flow, and suppose 1) that the local impact rate is the rate at which adjacent layers shear over each other; 2) that the force throughout an impact is described by Hertz theory with typical impact velocity equal to the standard deviation in particle velocity within each layer; and 3) that the Green's function includes exponential attenuation of the force with the impact's distance from the flow's base.

The use of Hertz theory to describe the contact force between impacting particles, detailed in Text S3, predicts the duration of impacts and so a frequency scale for the spectral density of the forces they exert (Hertz, 1881). For a collision at relative normal velocity u_n between two spherical particles of diameter d, consisting of material with density ρ, Young's modulus E, and Poisson's ratio ν, Hertz theory predicts a timescale for the impact

$$\tau = \left[\frac{\pi^2 \rho^2 (1-\nu^2)^2}{4E^2 u_n} \right]^{1/5} d. \tag{3}$$

With this τ, the spectral density of the normal force between the particles is

$$\left|\tilde{F}_I(f)\right|^2 = \left(\frac{\pi \rho d^3 u_n}{3} \right)^2 \zeta(\tau f) \tag{4}$$

for a non-dimensional function $\zeta(\tau f)$, plotted in Figure S6, which is approximately equal to 1 for $\tau f \ll 1$, monotonically decreases to $\zeta(\tau f_c) = 0.5$ for non-dimensional corner frequency $\tau f_c \approx 0.208$, and is much less than 1 for $\tau f > 1$. Impacts at higher velocities u_n apply forces with higher spectral density, over a wider frequency range.

This spectral density does not appear explicitly in Bachelet (2018) or Bachelet et al. (2021), which instead use the integral of ζ over all f to consider the total seismic power generated by a flow. However, we can follow the authors' reasoning to derive from Equation 4 a prediction for the spectral density of a flow's high-frequency landquake signal, in the form of Equation 1. First, separating a flow with representative particle size d and particle volume fraction ϕ into layers, and writing z_j for the vertical position of each layer and u_j for the mean horizontal velocity within it, the authors suggest that the rate of impacts is

$$n_I(\mathbf{x}) = \frac{4\phi}{\pi d^3}\sum_j (u_j - u_{j-1})\delta(z - z_j) \tag{5}$$

for Dirac delta function δ. Then, writing T_j for the granular temperature in the jth layer, equal to the variance of individual particles' velocities, the authors take the spectral density of the force applied by a typical impact to be given by Equation 4 with impact velocity $u_n = \sqrt{T_j}$. Finally, the magnitude of the frequency-space Green's function for an impact at height z is taken to be $e^{-\gamma z/2} \mid \tilde{G}_b \mid$, where γ is an attenuation constant and $\mid \tilde{G}_b \mid$, describing a measurement station's velocity response to vertical basal forces, is constant due to the assumption of an incoherent, diffuse seismic field with constant attenuation. Therefore, a flow of area A will generate a landquake signal with power spectral density

$$P_{v_{\mathbf{r}}}(f) = \frac{4\phi A}{\pi d^3}\left|\tilde{G}_b\right|^2 \sum_j (u_j - u_{j-1})\Delta p_j^2 \zeta(\tau_j f) e^{-\gamma z_i} \tag{6}$$

for

$$\Delta p_j = \frac{\pi\rho d^3\sqrt{T_j}}{3}, \quad \tau_j = \left[\frac{\pi^2\rho^2(1-\nu^2)^2}{4E^2\sqrt{T_j}}\right]^{1/5} d. \tag{7}$$

The experiments described by both Bachelet (2018) and Bachelet et al. (2021) show this model to be consistent with measurements of the seismic signals generated by approximately steady and uniform laboratory-scale granular flows, but the results are not conclusive. Releasing flows of $d = 2$ mm-diameter glass beads in a channel inclined at angles between 16.5° and 18.1°, accelerometers were used to estimate the total seismic power imparted to an isolated plate by overlying flows of depths between $15d$ and $20d$, and this power was compared to the prediction of Equation 6, with flow parameters estimated using high-speed photography through the channel's transparent sidewalls. The agreement is reasonable, but is highly dependent on the fitted parameter γ, and so the number of estimates, and their range of variation, are too small for conclusions to be definitive. The use of Hertz theory permits predictions for the frequency-dependence of the power spectral density, but no such predictions are compared with experimental results. Further tests are therefore required.

1.3. Aim of Our Work

Given their insufficient validation to date, our work aims to test the above models of high-frequency landquake signal generation. Because we are concerned with the generation of the signal, rather than its propagation, we consider models' predictions for the power spectral density P_F of the total base-normal force exerted by the flow, which may be obtained by removing the Green's function in Equation 1, so by dividing Equation 2 by $R^2e^{-2\alpha r}/r$ and Equation 6 by $\mid \tilde{G}_b \mid^2$. P_F will be proportional to the spectral density of the signal at a receiver, with its appropriately weighted integral proportional to the seismic power transmitted by the flow, but P_F, unlike these measurements, is independent of the response of the base on which the flow propagates.

However, it is difficult to use field-scale granular flows to test the models' predictions for P_F. Natural geophysical flows often occur in remote locations, infrequently and unpredictably, and so the sites of most flows are not instrumented for any measurements of flow parameters. Where sites are instrumented, the destructiveness of geophysical flows restricts which parameters can be measured, excluding most used by the above models. Furthermore, geophysical flows are typically extremely unsteady and heterogeneous, so that any given landquake signal may be produced by a flow region with parameters very different from those that have been measured. Finally, the inference from a landquake signal of the forces that generated it requires inversion of the Green's function, which is typically poorly constrained at the high frequencies of interest, and to which the inversion is typically very sensitive at precisely these high frequencies.

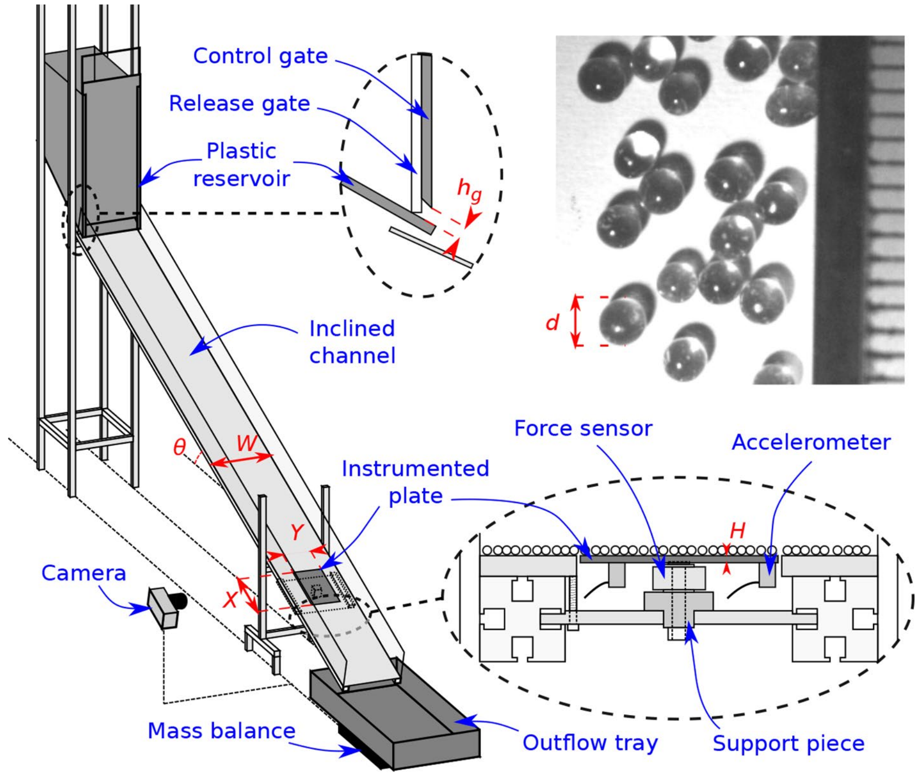

Figure 1. Schematic of experimental apparatus. Experiments are conducted in the channel represented, to scale, at left, with components of the apparatus labeled in blue and relevant dimensions in red. Expansions at top-center and bottom-right represent, in cutaway views and not to scale, details of the reservoir and the instrumented plate, respectively. The glass beads used in experiments are shown at top-right, with a mm-unit scale.

We therefore conducted laboratory experiments to link the properties of a granular flow to the seismic signal it generates. In the laboratory, flows can be fully controlled and instrumented, allowing a wide range of parameter values to be explored and measured. Apparatus can be designed to produce steady, fully developed, homogeneous flows, and the Green's function can be well constrained over a large frequency range by calibration. Since the models entirely neglect geophysical flows' fluid phases and consider normal impulses transferred between similarly sized particles, they can be tested with the dry flows of monodisperse, spherical grains that best satisfy their assumptions. Having established the relevant physics for simple flows, the applicability of results to more complex, geophysical flows can be discussed.

We describe our laboratory experiments in Section 2.1, our analysis of experimental data in Section 2.2, and our calculation of existing models' predictions for flows' force signals P_F in Section 2.3. Section 3.1 describes how each flow's signal evolves with the flow, over the course of an experiment, while Section 3.2 describes the properties of P_F and Section 3.3 compares those properties to the models' predictions. We discuss the implications of this comparison for our flows' velocity profiles in Section 4.1, and the relation between non-dimensional shear and non-dimensionalized force fluctuations in Section 4.2, while Section 4.3 discusses the application of our results to geophysical flows, including the effects of different Green's functions, particle size and polydispersity, and flow evolution. Section 5 concludes by summarizing our results.

2. Methods

2.1. Experimental Apparatus

As the simplest possible analog of a geophysical granular flow, we studied the flow of spherical glass beads, $d = 2$ mm in diameter, in an inclined channel 2.5 m long and $W = 0.2$ m wide, shown in Figure 1. The beads were 1.7–2.1 mm Type S glass beads produced by Sigmund Lindner GmbH and provided by MINERALEX, with material density $\rho = 2{,}500$ kg m^{-3} and Young's modulus $E = 63$ GPa (Sigmund Lindner, 2018). In each experiment, 40 kg of beads were initially stored in a plastic reservoir of volume 0.08 m^3, from which they flowed out via a rectangular opening of width 0.18 m and adjustable height h_g, controlled to within 0.06 mm by a plastic gate which was fixed in place during each experiment. A separate plastic release gate blocked this opening before each experiment and was manually lifted to start outflow. On leaving the reservoir, beads entered the separately supported channel, which had an aluminum base; transparent, 0.1 m-high acrylic walls; and an incline $\tan\theta$, which could be adjusted by changing the heights of the braces attaching the channel to its supports. The channel's base was roughened with the same type of glass beads as constituted the flow, fixed in place with extra-strong double-sided carpet tape, with an irregular, dense pattern achieved by random pouring.

The flow of beads down the channel adapted to these conditions over a distance of 1.92 m, before reaching a rectangular, instrumented steel plate set into a corresponding hole in the center of the channel's base. The plate was $X = 0.18$ m long, $Y = 0.1$ m wide, and $H = 2$ mm thick, with its surface flush with that of the aluminum base to within 0.02 mm and separated from it by an isolation gap of 0.04 ± 0.01 mm, achieved by using strips of plastic film as spacers during emplacement. The plate was supported by a force sensor and a support piece, with the three separated by washers and held together by a prestressing screw, the head of which was glued into a 0.5 mm-deep recess in the center of the plate's underside. The support piece, in turn, was attached to the channel's substructure using phenyl salicyclate (salol), which was added to the join when molten and solidified to form a stiff connection, but could be melted with a heat gun for removal of the plate or adjustment of its position. Before the plate's emplacement, we used the same salol to roughen its surface with glass beads: heating the plate, we added salol to form a thin, liquid layer, and we poured beads on top to form an irregular, dense pattern, before the salol solidified and fixed them in place.

After the plate, the flow of beads continued for 0.4 m, before flowing out of the channel and into a plastic outflow tray. Plastic sheeting extended the tray's walls, to prevent energetic particles from escaping.

Four sets of devices took measurements of the flow: a mass balance beneath the outflow tray; the force sensor supporting the instrumented plate; four accelerometers attached to the plate's underside; and a high-speed camera directed through the channel's wall. The mass balance was a Dymo S50 digital shipping scale, which measured in each experiment the cumulative mass that had passed through the channel. The force sensor was a Kistler 9027C three-component force sensor and was connected to a Kistler 5073 charge amplifier, measuring the normal, downslope, and cross-slope forces exerted by the flow on the plate. The accelerometers were Brüel and Kjær type 8309 accelerometers, attached with salol to randomly selected positions on the plate's underside and connected to a Brüel and Kjær Nexus 2692-A-OS4 conditioning amplifier, to measure the normal vibrations of the plate and hence the seismic energy imparted to it by the flow. Settings of the force sensor and accelerometer amplifiers are described in Text S4. The camera was an Optronis CR600x2, with a Sigma 17–50 mm F2.8 EX DC lens, and was level with and focused on the inside of the channel sidewall, directly cross-slope from the instrumented plate's center. The camera's inclination was the same as the channel's and its field of view was 640×256 pixels, corresponding to a region 8 cm long and 3.2 cm high. The sidewall was lit using a Photonlines H5 LED light, via a white sheet of paper which acted as a reflective diffuser, and we used an exposure of 250 μs and a frame rate of 2,000 s^{-1}.

To control the measurement devices, we used an Arduino Uno R3 microcontroller board, and we recorded measurements using a Pico Technology Picoscope 4824 oscilloscope connected to a Lenovo E530 laptop. Measurements from the mass balance, force sensor, and accelerometers were recorded from the time $t = 0$ at which the reservoir's release gate was lifted until the outflow stopped at $t = t_e$, while the camera recorded footage over a duration Δt_c between 2 and 10 s, after a delay time t_d in which the flow developed into a steady state. Details are in Text S5.

We conducted experiments with six different channel inclinations between 22.8° and 27.5° ($\tan\theta = 0.42$, 0.44, 0.46, 0.48, 0.50, and 0.52), with this order randomized to negate the effect of any systematic variation in atmospheric conditions or measurement sensitivity. For each inclination, we conducted three repeats with the reservoir control gate at each of four different heights ($h_g = 5$, 10, 20, and 40 mm), with the order of gate heights again selected at random.

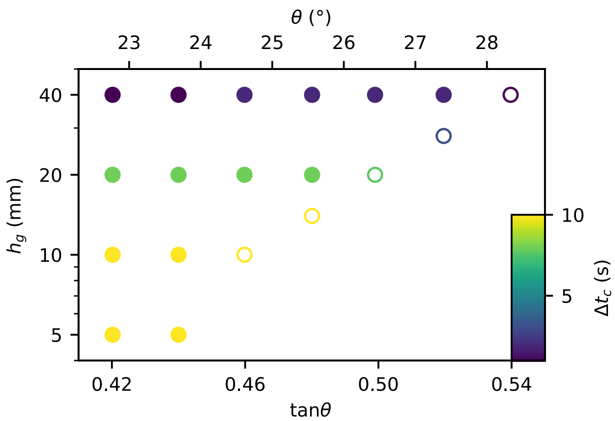

Figure 2. Channel inclines $\tan\theta$ and release gate heights h_g used in experiments. ∘ indicates an experiment for which the flow was in the transitional regime, while colors indicate the duration of time Δt_c recorded by the camera.

At channel inclines equal to and greater than $\tan\theta = 0.46$ ($\theta = 24.7°$), there was a gate height below which flows were in the gaseous regime of, for example, Börzsönyi and Ecke (2006) and Taberlet et al. (2007), with all glass beads in saltation and accelerating downslope. We recorded no measurements of such flows, which were energetic and far from stationary, with a large number of beads escaping across the channel's sidewalls and with the camera's images unusable for reliable measurements. At each such incline, we instead recorded measurements at all gate heights resulting in dense flows and at one gate height resulting in a "transitional-regime" flow, with a dense basal flow below a saltating layer. These gate heights are plotted in Figure 2, within the full parameter space investigated.

2.2. Data Analysis

For each experiment within the parameter space, we analyzed the experimental data to calculate dynamic, seismic, and kinematic properties of the flow: the mass of particles that lay over the instrumented plate and the effective friction coefficient between the two; the mass flux of particles through the channel and their average velocity; the power spectrum of the normal force exerted on the plate by the flow; and the vertical profiles of particle volume fraction, velocity, and granular temperature at a channel wall. We recall that W denotes the channel's width and θ its angle of inclination; that X, Y, and H denote the length, width, and thickness of the plate; and that t_d and Δt_c denote the delay before and the duration of the high-speed camera's recording, respectively. These and all other variables are listed in Text S1 and all code used to perform these analyses is available at Arran et al. (2021).

To infer the mass overlying the plate and its effective friction coefficient with the flow, we used the data from the force sensor. Averaging over successive 0.5 ms intervals, the net downslope force $F_x(t)$ and plate-normal, downwards force $F_z(t)$ applied to the plate by the flow were calculated from the voltage output of the force sensor's charge amplifier, as described in Text S6. Then, assuming no net plate-normal acceleration of the flow overlying the plate, over the period of steady flow recorded by the camera, we calculated the average mass per unit area overlying the plate as

$$\sigma = \frac{\langle F_z \rangle_{\Delta t_c}}{XYg\cos\theta}, \tag{8}$$

where $\langle \cdot \rangle_{\Delta t_c}$ represents the arithmetic mean over $t_d < t < t_d + \Delta t_c$ and g represents gravitational acceleration. Similarly, we followed Hungr and Morgenstern (1984) and Roche et al. (2021) in calculating the effective friction coefficient as

$$\mu = \frac{\langle F_x \rangle_{\Delta t_c}}{\langle F_z \rangle_{\Delta t_c}}, \tag{9}$$

with this calculation validated in Section S6.3.

To calculate the mass flux through the channel, we examined the data recorded by the mass balance. Having the cumulative mass $M(t)$ that had flowed through the channel after time t, we calculated the average flux per unit channel width, over the period of steady flow recorded by the camera, as

$$q = \frac{M(t_d + \Delta t_c) - M(t_d)}{\Delta t_c W}. \tag{10}$$

Assuming this average mass flux to be equal to that across the plate, and having calculated the mass overlying the plate, we could then calculate the mean depth-averaged flow velocity across the plate,

$$\bar{u} = q / \sigma. \tag{11}$$

To extract the power spectral density of the flow's basal force, we processed data from the accelerometers using Kirchhoff-Love plate theory (Love & Darwin, 1888) and assuming perfect isolation of the plate from the channel and linear attenuation within the plate. On the basis of the steel's technical documentation (John Steel, 2019; Steel, 2019), we took its density to be $\rho_p = 7{,}800$ kg m^{-3}, its Young's modulus to be $E_p = 200$ GPa, and its Poisson's ratio to be $\nu_p = 0.29$. Then, its bending stiffness was $D = E_p H^3 / 12(1-\nu_p^2)$ and the mean gap between the resonant frequencies at which its motion was sensitive to forcing was $\Delta_f = 2\sqrt{D} / XY\sqrt{\rho_p H} \approx$ 400 Hz. Assuming that the spectral density of an impact's force varied little over this frequency scale, this spectral density was estimated using D, the proportion of the plate's energy $\mathcal{P}$ in its steel structure's vertical displacements, the quality factor Q describing the attenuation of energy in the plate, and the accelerations $a_j(t)$ measured by the four accelerometers, as

$$P_F(f) = \frac{\left|\tilde{F}(f)\right|^2}{\Delta t} \approx \frac{(\rho_p H)^{3/2} XY\sqrt{D}}{\pi \mathcal{P} Q f \Delta t} \langle \sum_{j=1}^{4} \left|\tilde{a}_j(f)\right|^2 \rangle_{\Delta f}, \tag{12}$$

where Fourier transforms are over a time interval $\Delta t = 0.2$ s, and $\langle \cdot \rangle_{\Delta f}$ represents a moving average over frequency, with window width $\Delta f = 2$ kHz. We describe in Section S7.1 the derivation of this relation and the calculation of $\left|\widetilde{a_j}\right|^2$ from the voltage output of the accelerometers' conditioning amplifier; in Section S7.2, the calibration we performed to measure the plate parameters $\mathcal{P} = 0.25$ and $Q = 99$ and to extend the flat frequency range of the accelerometers to 120 kHz; and in Section S7.3 the validation of this work. The gaps between the plate's resonant frequencies limit both the resolution and the lower limit of our P_F-measurements to 1 kHz, whilst an accelerometer resonance at 125 kHz prevents measurement above 120 kHz. Measurements have a frequency-dependent, systematic relative error of typical magnitude around 40%, due to an imperfect attenuation model and variation in the number of resonant frequencies within each 2 kHz interval.

Finally, to extract profiles of kinematic properties at the channel wall, we analyzed the images taken by the high-speed camera, using particle tracking velocimetry and Gaussian coarse-graining. Analyzing each frame in turn, we detected the positions (x_j, z_j) of particles at the channel walls and, tracking particles between consecutive frames, calculated their mean velocities over each 0.5 ms interval. Calculating the smoothed velocities $\mathbf{u}_j$ over five frames, or 2.5 ms, we estimated the downslope-averaged and time-averaged base-normal profiles at the channel's wall of relative volume fraction $\phi_w(z)$, mean velocity $\mathbf{u}_w(z)$, and granular temperature $T_w(z)$ as

$$\phi_w(z) = \langle \sum_j C(z_j; z)\pi d^2 / 4 \rangle_{\Delta t_c}, \tag{13}$$

$$\mathbf{u}_w(z) = \langle \sum_j C(z_j; z)\pi d^2 \mathbf{u}_j / 4 \rangle_{\Delta t_c} / \phi_w(z), \tag{14}$$

$$T_w(z) = \langle \sum_j C(z_j; z)\pi d^2 \parallel \mathbf{u}_j - \mathbf{u}_w(z) \parallel^2 /4 \rangle_{\Delta t_c} / \phi_w(z), \tag{15}$$

where averages are over all frames recorded by the camera, sums are over all particles tracked in each frame, and C is a Gaussian weight function, localized around z and with integral over the total spatial domain equal to 1. This process is described in detail in Section S8.

While the irregularity of the flow's base and surface complicate the definition of the flow thickness h, we take the base-normal co-ordinate z to be zero at the top of the base's fixed beads, and extract h as the value of z at which $\phi_w(z)$ drops below half its maximum value,

$$h = \min\{z > \operatorname{argmax} \phi_w \mid \phi_w(z) < \max(\phi_w) / 2\}. \tag{16}$$

For a flow with constant particle volume fraction below a level surface, this exactly corresponds to the intuitive flow depth. While other reasonable definitions lead to different values of h and of all quantities derived from it, they do not alter our conclusions.

2.3. Model Predictions

For each of the models described in Section 1.2, for a granular flow's seismic signal, we inferred predictions for the experimental seismic signal. Specifically, we expressed a prediction $\hat{P}_F$ for the power spectrum of the base-normal force applied by the flow to the instrumented plate, as a function of the flow properties specified in Section 2.2: the mean depth-averaged flow velocity $\bar{u}$, the mass overburden per unit area σ, the flow depth h, and the channel-wall profiles $u_w(z)$ and $T_w(z)$ of downslope velocity and granular temperature. Since previous authors attempted to predict slightly different seismic properties and used slightly different flow properties, no directly applicable expressions are in the articles introducing the models (Bachelet, 2018; Farin, Tsai, et al., 2019; Kean et al., 2015; Lai et al., 2018). We therefore worked from Equation 2 and 6; used the models' methods of estimating those equations' variables, as described in Sections 1.2.1 and 1.2.2; and removed Green's functions as described in Section 1.3, to predict the basal force's power spectrum rather than the power spectrum of a seismic station's response. Recalling that $g\cos\theta$ denotes base-normal gravitational acceleration, d the particles' mean diameter, and ρ their density, and approximating the flow area generating the measured signal by the instrumented plate's area $A = XY$ and the flow's mean volume fraction by $\phi = \sigma/\rho h$, these predictions could then be compared to the measured power spectra P_F.

The model introduced by Kean et al. (2015) predicts the seismic signal generated by a granular flow covering a certain area, using its surface velocity and the base-normal component of its weight per unit area. If the near-base velocity of the flow scales with its surface velocity, as Kean et al. (2015) suggests, then both will scale with the depth-averaged velocity $\bar{u}$, so to calculate predictions we estimated the velocity u of Equation 2 with $\bar{u}$ and the impulse Δp with $\sigma g\cos\theta$, the measured base-normal component of the flow's weight per unit area. We may therefore write the model's prediction for P_F, for signal periods $1/f$ well above the duration of a typical impact, as

$$\hat{P}_F^0 = KA\bar{u}(\sigma g\cos\theta)^2 / d^3. \tag{17}$$

K is a free parameter, which in Kean et al. (2015)'s model is equal to the product of a constant volume fraction; a constant of proportionality between $\bar{u}$ and the near-base flow velocity; and a squared constant of proportionality between the mean basal pressure and the typical impulse transferred by a basal impact. No indication is given as to its value, so it must be found by fitting.

In contrast, the model introduced by Lai et al. (2018) requires no free parameter. Noting that the experimental particles have a narrow diameter distribution, with 94th percentile approximately equal to its mean d, and using the appropriate substitutions for u and Δp in Equation 2, the model's prediction for P_F is the constant

$$\hat{P}_F^0 = \pi^2\rho^2 A d^3\bar{u}^3 / 9, \tag{18}$$

with the implicit assumption that the volume fraction is equal to 1. Again, this prediction is expected to be valid only for signal periods $1/f$ well above the duration of a typical impact.

The two models described by Farin, Tsai, et al. (2019) are developments of this model, with that article's Equation 16 developing the definition of the impulse denoted Δp in our Equation 2. Within the same frequency range as in prior paragraphs, the associated predictions for $P_F(f)$ are the constants

$$\hat{P}_F^0 = \pi^2\rho^2\phi A d^3(1+e)^2\xi(\upsilon)u_b^3 / 36, \tag{19}$$

where e is a constant coefficient of restitution; $\xi(\upsilon) \approx 0.053(1 + 5.6\upsilon^2)$ is a non-dimensional function accounting for variation in impacts' geometry; and υ and u_b define the velocities of base-impacting particles $u_b(\mathbf{e}_x + \upsilon\mathbf{e}_\upsilon)$, for randomly directed unit vector $\mathbf{e}_\upsilon$.

In the "thin-flow" model, $u_b = \bar{u}$, whereas in the "thick-flow" model $u_b = \chi\bar{u}d / h$ for velocity profile shape factor χ, assumed constant and between 1 and 1.5. The model-specific parameters are e, υ, and χ, which can neither be reliably measured in individual experiments nor individually determined via fitting. We therefore take $e = 0.9$, consistent with the rebound heights of particles dropped onto the instrumented plate; take $\chi = 1.25$, consistent with the velocity profiles measured at the channel's wall and introducing an error factor of at most 2; and fit the free parameter υ, corresponding to the normalized standard deviation of base-impacting particles' velocities. Farin, Tsai, et al. (2019)'s derivation of ξ makes unphysical assumptions (e.g., that impacting particles' velocities differ from $u_b\mathbf{e}_x$ by an exactly constant magnitude υu_b and that, for each impact velocity, all possible impact locations are equally likely), so the best fit value of υ for an otherwise-accurate model will not exactly equal the true normalized standard deviation, but a model cannot be said to be accurate unless this best fit value is a physically reasonable approximation. Specifically, the energy associated with velocity fluctuations is drawn from the mean flow and dissipated rapidly, so that we expect the typical magnitude of velocity fluctuations to be less than the mean velocity, and hence a condition for model accuracy is that $\upsilon < 1$.

To further assess the assumptions of the "thick-flow" and "thin-flow" models, we extended each model to higher frequencies. Farin, Tsai, et al. (2019) assumes binary, elastic, normal interactions during impacts, with impact velocities such that particle deformation in our experiments will be quasistatic and the Hertz theory described in Text S3 will apply. Applying this theory to the impact velocities and geometry assumed by Farin, Tsai, et al. (2019), we therefore compute predictions for P_F over a larger frequency range than that considered by the original article, as

$$\hat{P}_F(f) = \frac{\int_{S^2} \mathrm{d}^2\mathbf{e}_\upsilon \int_{S^2_{\pi/6}} \mathrm{d}^2\mathbf{e}_n \left(u_n\mathbf{e}_n\cdot\mathbf{e}_z\right)^2 \zeta(\tau f)\mathcal{H}\left(u_n\right)}{\int_{S^2} \mathrm{d}^2\mathbf{e}_\upsilon \int_{S^2_{\pi/6}} \mathrm{d}^2\mathbf{e}_n \left(u_n\mathbf{e}_n\cdot\mathbf{e}_z\right)^2 \mathcal{H}\left(u_n\right)} \hat{P}_F^0 \tag{20}$$

for unit sphere S^2; unit spherical cap $S^2_{\pi/6}$ with maximum polar angle $\pi/6$; normal impact velocity $u_n = u_b(\mathbf{e}_x + \upsilon\mathbf{e}_\upsilon)\cdot\mathbf{e}_n$; impact timescale $\tau(u_n)$ as defined by Equation 3; non-dimensional function ζ as introduced in Equation 4; and Heaviside step function $\mathcal{H}$.

Finally, the model of Bachelet et al. (2021) already predicts P_F over a large frequency range. Substituting Equation 7 into 6 and moving from the well-defined particle layers considered in the thesis to the continuous profiles measured in our experiments, the predicted power spectral density of the basal force is

$$\hat{P}_F(f) = \frac{4\pi}{9}\phi A\rho^2 d^3 \int_0^h u_w'(z)T_w(z)\zeta\left(\tau_w(z)f\right)e^{-\gamma z}\,\mathrm{d}z, \tag{21}$$

where u'_w is the derivative of u_w with respect to z; ζ is the non-dimensional function in Equation 4; impact timescale $\tau_w(z)$ is defined with respect to $T_w(z)$ as τ_j is to T_j in Equation 7; and constant γ is a free parameter, to be determined by fitting.

We compare these predictions to the measured power spectra P_F in Section 3.3, but first we define the time period and the frequency-space properties used for the comparison, by considering the evolution of the flow (Section 3.1) and the form of the power spectrum of the basal force (Section 3.2).

3. Results

3.1. Evolution of the Flow

In each experiment, the flow passing a given point evolved through four stages that could be distinguished from measurements of outflow mass M and the net normal force on the plate F_z: I) precursory saltation of particles released at the start of the experiment; II) arrival of the dense flow's front; III) steady flow; and IV) decay of the flow. These corresponded to different signals measured at the instrumented plate, as illustrated for two different experiments in Figure 3.

As Figure 3 illustrates, saltating particles in stage I contributed little to the outflow mass M and to the net downslope and normal forces F_x and F_z, with an implied number density of around one particle per cm^2 of plate surface, but such particles applied basal forces with significant spectral density P_F across a wide frequency range. Similarly, the dense front's arrival in stage II had a short duration, but was associated with an intense, broad power spectrum of basal force, as high-velocity, surficial particles reached the front and impacted the plate. In general, as in Figure 3a, the power spectrum at high frequencies then dropped during stages III and IV, indicating that impact velocities in the dense flow's bulk were lower than those

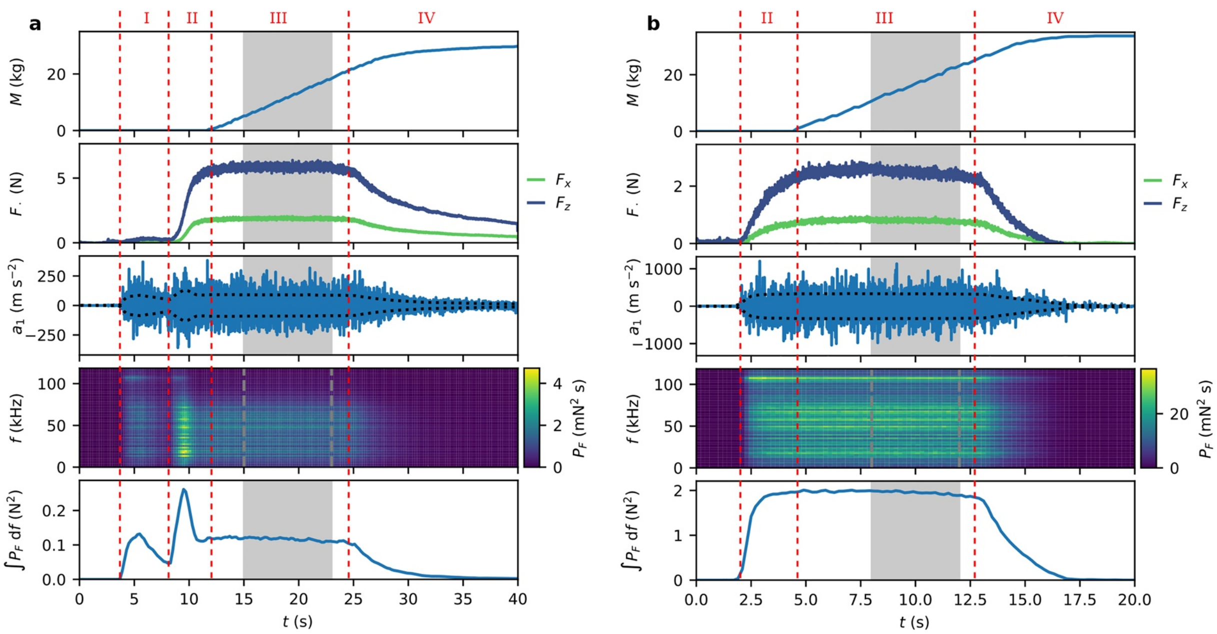

Figure 3. Examples of flow properties' evolution over time. Plots over time t of the cumulative outflow mass M; the net downslope and normal forces F_x and F_z applied to the instrumented plate; a measured normal plate acceleration a_1, with envelope indicated by dotted lines; the power spectral density P_F of the plate-normal basal force; and the integral of this power spectrum, which Equation 12 shows to be proportional to the seismic power transmitted to the instrumented plate. (a) A dense flow at a channel incline $\tan\theta = 0.44$ ($\theta = 23.7°$), with a release gate height $h_g = 20$ mm. (b) A transitional-regime flow, with $\tan\theta = 0.52$ ($\theta = 27.5°$) and $h_g = 28$ mm. Flow stages I–IV are labeled, where present, and the shaded region indicates the period of steady flow recorded by the camera, $t_d < t < t_d + \Delta t_c$.

of high-velocity saltating particles. For "transitional-regime" flows, however, P_F remained the same during stages II and III, as in Figure 3b, reflecting the continued saltation within each flow that defines this regime.

Such variation of signal properties between different experiments is summarized in Table 1. With increasing channel incline $\tan\theta$ and release gate height h_g, the duration of stage I decreased rapidly and that of stage II decreased slightly, as the speed of the dense flow front increased to the speed of saltating particles. Since the same changes greatly increased the high-frequency spectral density P_F of the plate-normal force during stage III, which had duration determined by the reservoir's capacity and decreasing with h_g, the contribution of stage I to the total generation of seismic energy decreased from around 70% to less than 0.1%, while the contribution of stage II remained between around 10% and 20%, and the contributions of stages III and IV increased. In contrast to this pattern of variation, the net normal force F_z increased with h_g but, for each h_g, decreased with increasing $\tan\theta$; the same h_g-determined flux of particles was maintained by faster flows, which were therefore thinner. These opposing trends indicate the independence of F_z and $P_F(f)$ for $f \neq 0$, with the former the mean force applied by the flow, and the latter associated with the force's fluctuations about this mean.

Table 1
Properties of the Flow's Stages of Evolution

Flow stage	I	II	III	IV
Durations (s)	0–40	2–8	4–150	5–20
F_z (N)	$O(0.1)$	0 → (1–10)	1–10	(1–10) → (0–2)
f_c (kHz)	>100	>90	•70–110 ∘>100	•70–110 ∘>100
$\int P_F$ df (N^2)	$O(0.1)$	0.02–2	0.003–3	(0.003–3) → 0

Note. F_z and P_F are as defined in Section 2.2, while f_c is the frequency at which P_F drops to half its mean value pre-maximum. Arrows (→) indicate ranges over time in an experiment, while hyphens (–) represent the ranges over different experiments. • indicates the value for dense flows and ∘ for transitional-regime flows, wherever they differed significantly.

In this article, we restrict our attention to stage III of the flow's evolution, in which the flow's steadiness ensured that all measurements were of the same flow state. Specifically, between different $\Delta t = 0.2$ s time intervals within the duration Δt_c of steady flow recorded by the camera, the per-second rate of change of outflow mass M had a standard deviation of around 10% of its mean value, while the standard deviations of F_x and F_z were around 1% and that for $\int P_F$ df around 5%. Similarly, we examined the profiles of kinematic properties at the channel wall, averaged in turn over each decile of time $t_d + n\Delta t_c/10 < t < t_d + (n+1)\Delta t_c/10$ within the period recorded by the camera. Within the flow, kinematic properties at the channel wall were steady over time, in the sense that the values of

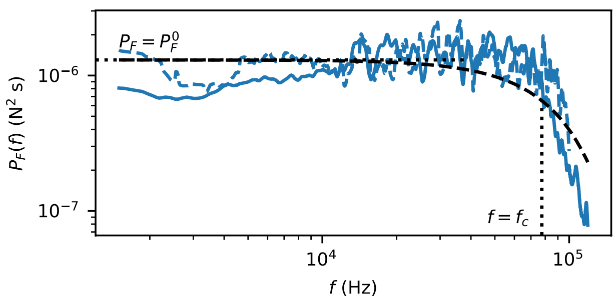

Figure 4. Example of the plate-normal force's power spectral density during steady flow. The measured power spectrum (blue, solid line) corresponds to the same experiment as Figure 3a, with channel incline $\tan\theta = 0.44$ ($\theta = 23.7°$) and release gate height $h_g = 20$ mm. The dotted lines indicate the corner frequency $f_c = 77.5$ kHz and the low-frequency amplitude P_F^0 =1.29 mN^2 s. The black dashed line indicates the Hertzian power spectrum fit to these values, closely approximating the functional form predicted by the model of Bachelet et al. (2021) and by our extensions of Farin, Tsai, et al. (2019)'s models. It was calculated from Equations 3 and 4 and corresponds to 4,000 Hertzian impacts per second, each at normal velocity $u_n = 0.9$ m s^{-1}, of the $d = 2$ mm experimental particles on the plate's surface. The blue dashed line represents a "corrected" power spectrum, calculated with Section S7.3's estimate for the frequency-dependent systematic relative error.

$\phi_w(z)$, $\mathbf{u}_w(z)$, and $T_w(z)$ varied by at most a few percent over time, for each z satisfying $\phi_w(z) > \max_z \phi_w(z)/2$.

3.2. Power Spectrum of the Basal Force

Averaging over this period of steady flow, by taking $\Delta t = \Delta t_c$ in Equation 12, we calculated the power spectrum of the base-normal force applied by the flow to the plate and find it to be consistent with impacts of short duration. As in the example shown in Figure 4, the power spectral density $P_F(f)$ is approximately constant over a large frequency range and displays the same decay beyond a given corner frequency as Hertz theory predicts for a single impact. The high, O(100 kHz) corner frequencies are comparable to those predicted by Equation 3 for the small, O(1 mm) experimental particles, while the deviations from power spectra proportional to Equation 4 are consistent between experiments and generally consistent with the systematic errors discussed in Section 2.2, as estimated in Section S7.3.

We described the power spectrum by two quantities: its low-frequency amplitude P_F^0 and its corner frequency f_c. We calculated f_c as the frequency at which $P_F(f)$ drops to half its mean pre-maximum value, so that for errorless measurement of a Hertzian impact it would be equal to ~$0.208/\tau$, for the impact timescale τ defined by Equation 3. The systematic errors in $P_F(f)$ will result in systematic error in f_c of order 20%, for which we are unable to compensate with our uncertain error estimates. However, our measurements of f_c were sufficiently robust that we calculated P_F^0 as the arithmetic mean value of P_F over all frequencies less than $f_c/2$, with systematic errors in P_F canceling out over this range. We could then compare these experimentally measured values with the model predictions, computed as described in Section 2.3.

3.3. Tests of Existing Models for Flows' Seismic Signals

To assess the model predictions described in Section 2.3, we compared their predictions $\hat{P}_F^0$ for the low-frequency value of the basal force's power spectrum to the measured values P_F^0. Where possible, we also inferred a prediction $\hat{f}_c$ for the corner frequency of the basal force's power spectrum, as the frequency at which $\hat{P}_F(f)$ dropped to half its maximum value, and we compared this prediction with the measured value f_c. Where a model had a free parameter, we used the parameter value that minimized the sum over all experiments of $\ln(P_F^0 / \hat{P}_F^0)^2$, which was equivalent to minimizing the typical logarithmic error or maximizing the model likelihood under the assumption that measurements were log-normally distributed about their predicted values (see Text S9). Table 2 lists these best fit parameter values and Figure 5 shows the results of the comparisons.

The model introduced by Kean et al. (2015) predicts P_F^0 poorly, due largely to its incorrect assumption of proportionality between the pressure fluctuations relevant to P_F^0 and the mean pressure $\sigma g \cos\theta$ used as input. To best fit the measurements, the free parameter K had to take a value of 4.0×10^{-16} m^4 s^2, entirely unpredicted by the model, and even then predictions often differed from measurements by an order of magnitude (Figure 5a). Notably, the model's predictions $\hat{P}_F^0$ decrease for flows at higher channel inclinations or in the transitional regime, for which the mean pressure is lower, whereas such flows' higher impact energies in fact resulted in higher pressure fluctuations and so larger measured values P_F^0.

In contrast, the model introduced by Lai et al. (2018) accurately predicted variation in P_F^0 between experiments, with predictions for dense flows consistently 3–10 times larger than the measured values (Figure 5b). For transitional-regime flows, the predictions' errors are larger, due to the model's implicit assumption that the volume fraction is equal to one.

Of the two models described by Farin, Tsai, et al. (2019), the model derived for flows thicker than the largest particles is less accurate than that derived for thin flows, with the former's fit to observations requiring

Table 2
Summary of Model Testing

Model	Inputs	Equation	Best fit parameter	ϵ
Kean et al. (2015)	$\bar{u}, \sigma, \theta$	17	$K = 4.0 \times 10^{-16}\,\mathrm{m}^4\,\mathrm{s}^2$	4.2
Lai et al. (2018)	$\bar{u}$	18	n/a	18.5
Farin, Tsai, et al. (2019)	$\bar{u}, \sigma, h$	19		
"Thick-flow"			$\upsilon = 9.8$	3.2
"thin-flow"			$\upsilon = 0.51$	2.1
Bachelet et al. (2021)	σ, h, u_w, T_w	21	$\gamma = 0\,\mathrm{m}^{-1}$	3.9

Note. For each of the existing models described in Section 1.2, we list the flow measurements defined in Section 2.2 that are required to predict the flow's high-frequency seismic signal. We further record the equation for predictions $\hat{P}_F^0$; the free parameter value for which such predictions best fit measurements; and the geometric standard error $\epsilon = \exp\left[\sqrt{\frac{1}{N}\sum \ln(P_F^0 / \hat{P}_F^0)^2}\right]$ of these predictions.

an unrealistically large ratio υ between the magnitudes of velocity fluctuations and of the mean velocity. As explained in Section 2.3, realism demands that $\upsilon < 1$, but the "thick-flow" model requires $\upsilon = 9.8$ for predictions $\hat{P}_F^0$ to be as large as measurements P_F^0 and, in that case, the predictions are too large for the transitional-regime flows (Figure 5c). For the "thin-flow" model, meanwhile, the best fit value is $\upsilon = 0.51$, which is physically reasonable and provides an excellent fit of $\hat{P}_F^0$ to P_F^0 over all experiments (Figure 5d).

This difference between the "thick-flow" and "thin-flow" models' best fit values of υ is reflected in the predictions $\hat{f}_c$ they implied for the corner frequency of the basal force's power spectrum, calculated according to our extensions of these models using Equation 20. The higher υ required for the "thick-flow" model results in higher predictions $\hat{f}_c$, matching the measured values f_c (Figure 5f), whereas for the "thin-flow" model predictions are consistently ~30% smaller than the measured values (Figure 5g). Predicted corner frequencies $\hat{f}_c$ are as large as measurements f_c only for typical impact velocities 6 times larger than the flows' mean velocities, suggesting that our measurements f_c were slight, but systematic, overestimates. Such systematic disagreement is consistent with the systematic errors in P_F discussed in Sections 2.2 and 3.2, or with 30% error in the particle properties in Equation 3.

Finally, the predictions of the "Bachelet et al." model followed the correct trend but had a wide dispersion (Figure 5e). The free parameter γ, representing signal attenuation within the flow, had best-fit value 0, indicating that the unattenuated contributions of all synthetic impacts are necessary for $\hat{P}_F^0$ to be large enough to compare to P_F^0. Even then, the lower energies of synthetic impacts are reflected in predictions $\hat{f}_c$ for the power spectrum's corner frequency that are even lower than those of our extension to Farin, Tsai, et al. (2019)'s "thin-flow" model (see Figure 5h).

Overall, of the five models, the "thin-flow" model described in Farin, Tsai, et al. (2019) best fits the results from our experiments. While the fit is imperfect, the predictions $\hat{P}_F^0$ of this model differ from the measured values P_F^0 by a typical factor of 2.1, lower than that for the other models, and the model's accuracy is approximately equal across the entire range of experiments, including for the flows in the transitional regime. Constructing a statistical model for each physical model, by assuming $\ln P_F^0$ was normally distributed about $\ln \hat{P}_F^0$ with constant variance, the "thin-flow" model is also the preferred model by the Akaike information criterion (see Text S9), indicating that its additional free parameter compared to the Lai et al. (2018) model is worthwhile in an information theoretic sense. This analysis did not compare models' predictions to the measured corner frequencies f_c, due to the likelihood of systematic error in the latter, but our extensions to the models of Farin, Tsai, et al. (2019) both predicted a trend in $\hat{f}_c$ consistent with measurements.

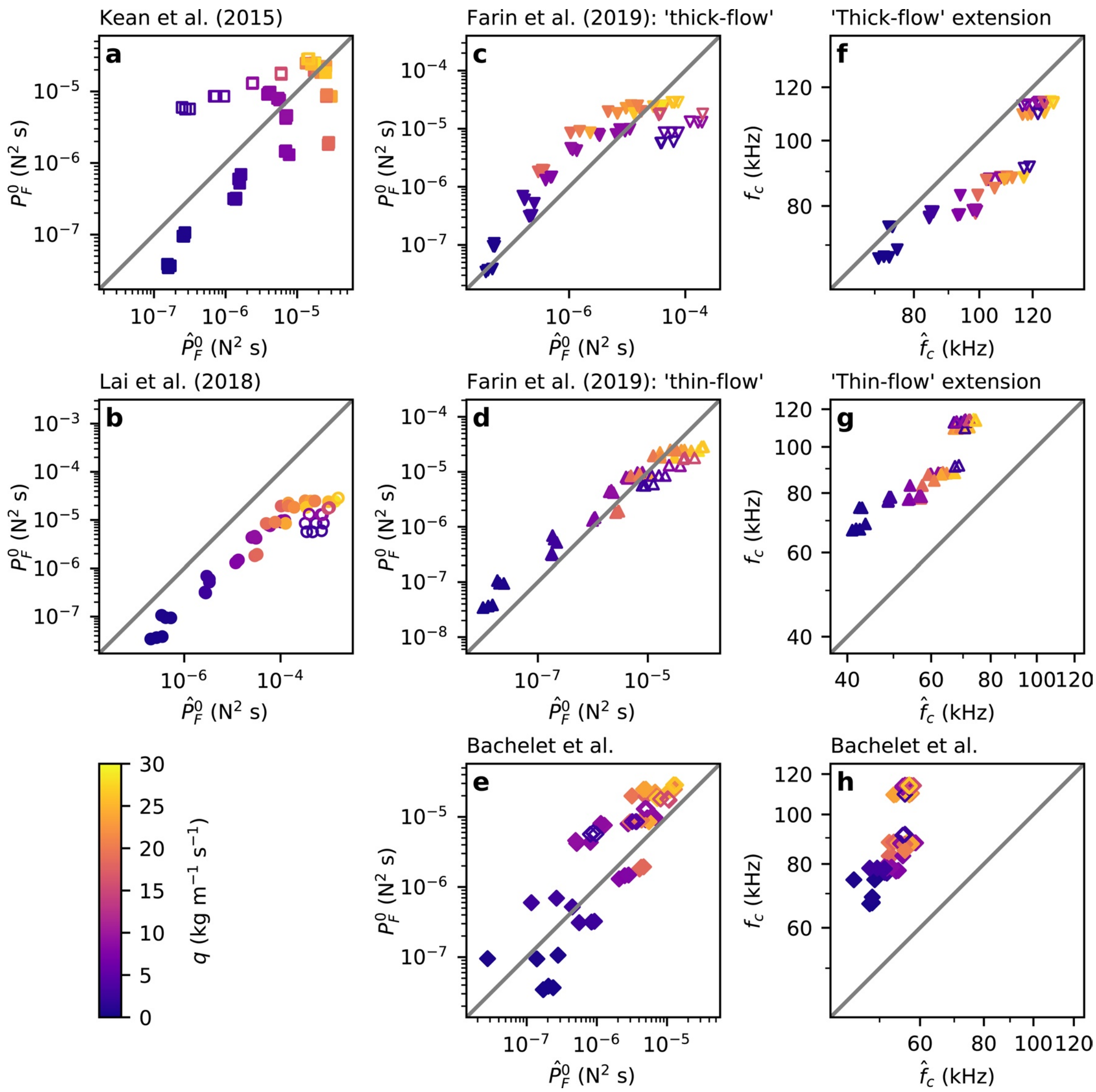

Figure 5. Comparison between models' predictions (*x*-axes) and experimental measurements (*y*-axes) for the basal force's power spectrum during steady flow. Plots f, g, and h represent predictions for the corner frequency of the basal force's power spectrum, while all others represent predictions for the power spectral density's value at frequencies well below this corner frequency. In all plots, the gray line represents perfect agreement between predictions and measurements, colors indicate each experiment's mass flux q per unit channel width, and unfilled symbols represent experiments for which the flow was in the transitional regime.

4. Discussion

4.1. Velocity Profiles and the “Thin-Flow” Model

That the “thin-flow” model best predicts the experimental results is surprising, because we do not expect the velocity profile within the flow to be consistent with the model's assumptions. The “thin-flow” model assumes that particles at the flow's base move across the instrumented plate's surface at approximately the flow's mean velocity, whereas previous authors suggest that the plate's roughened surface should impose a no-slip condition on the flow, in the sense that particles' velocities should tend to zero toward the flow's base (GDR; Jing et al., 2016; MiDi, 2004). Furthermore, as the example of Figure 6 demonstrates, the velocity profiles we observe at the channel's wall are consistent with this no-slip condition (which we note is distinct from any micromechanical condition on rolling or sliding at particle contacts).

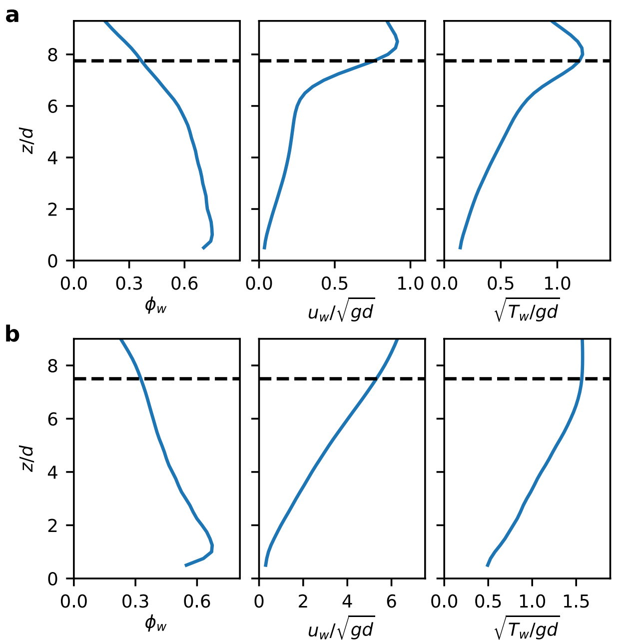

Figure 6. Examples of kinematic properties' steady profiles at the channel wall. Profiles are estimates from particle tracking velocimetry of the relative volume fraction ϕ_w, the downslope velocity u_w, and the square root $\sqrt{T_w}$ of the granular temperature, non-dimensionalized by $\sqrt{gd} = 0.14$, while the dashed lines represent the flow thicknesses h inferred from the profile of ϕ_w. Profiles are taken from the same experiments as for Figure 3: (a) a dense flow at channel incline $\tan\theta = 0.44$ ($\theta = 23.7°$) with release gate height $h_g = 20$ mm. (b) A transitional-regime flow at channel incline $\tan\theta = 0.52$ ($\theta = 27.5°$) with release gate height $h_g = 28$ mm.

We propose two possible explanations for the success of the "thin-flow" model. The first is that the instrumented plate's flow-induced vibration reduces the effective friction between it and the flow, leading to basal slip and a basal flow velocity closer to the flow's mean velocity. The second is that basal particles have low velocities, but that impacts away from the flow's base make significant contributions to the basal force exerted by the flow, in such a way that the total contribution of these impacts scales with the mean velocity of the flow.

The first explanation is supported by the literature on frictional weakening and by measurements of the plate's effective friction coefficient with the flow. The reduction by vibration of a granular medium's effective friction has been documented in discrete element simulations (e.g., Capozza et al., 2009; Ferdowsi et al., 2014; Lemrich et al., 2017) and experiments (e.g., Dijksman et al., 2011; Johnson et al., 2008; Lastakowski et al., 2015; Léopoldès et al., 2020), with suggestions for the necessary vibration amplitude being a particle strain of order 10^{-6} (Ferdowsi et al., 2014), a velocity of order 100 μm s^{-1} (Lastakowski et al., 2015), and an acceleration of order 0.1 g (Dijksman et al., 2011). Even in the experiments in which the plate vibration amplitudes during steady flow were lowest, the plate had approximate root mean square normal displacement 10 nm, velocity 100 μm s^{-1}, and acceleration 20 ms^{-2} (around an order of magnitude larger than were measured away from the plate), so a vibration-induced reduction in friction appears viable. Furthermore, the effective friction coefficients μ that we measure between the plate and the flow are too low to prevent basal slip on the surface of the plate, with Figure 7a showing that $\mu < \tan\theta$ for all channel inclines $\tan\theta$. This implies that basal particles accelerate across the plate's surface, toward the flow's mean velocity.

On the other hand, we do not directly measure any increases in velocity associated with basal slip. Over the 8 cm distance downslope captured by the high-speed camera, averaging over each flow's depth and each 4 cm half-window, the mean downslope velocities measured at the sidewall are uniform to within 10%. Away from the sidewalls, Tsang et al. (2019) suggests that a granular flow will adjust to a change in basal boundary conditions over a lengthscale of order $\bar{u}^2 / g$, for mean flow velocity $\bar{u}$ and gravitational acceleration g. This lengthscale varies in our experiments from 0.5 mm to 0.1 m, so that we would expect the effects of any basal slip to become evident at the flow's surface within the length of the instrumented plate. However, having

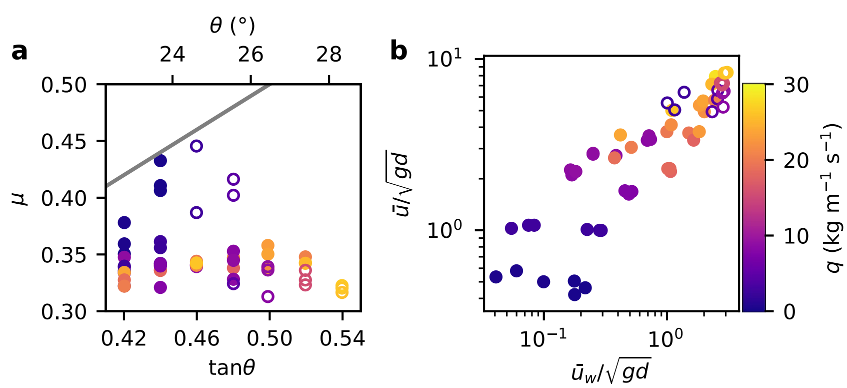

Figure 7. Complications in modeling the granular flow. (a) Measurements of the effective friction coefficient μ between the instrumented plate and the flow fall consistently below the condition $\mu = \tan\theta$ for zero basal slip (gray line). (b) The depth-averaged particle velocity measured at the channel wall $\bar{u}_w$ is poorly correlated with the mean velocity $\bar{u}$ calculated from bulk flow properties. Colors indicate each experiment's mass flux q per unit channel width, and unfilled symbols represent experiments for which the flow was in the transitional regime.

10.1029/2021JF006172

conducted particle image velocimetry with images captured by an overhead camera, for a flow at a channel incline $\tan\theta = 0.46$ ($\theta = 24.7°$) and with release gate height $h_g = 20$ mm, we were unable to distinguish whether the flow's surface's slight acceleration across the plate was induced by the plate, or was simply a continuation of the flow's acceleration toward a uniform state. Similarly, we attempted to detect changes in the velocity of basal particles, via Jop et al. (2005)'s method of examining soot erosion from an inserted metal plate, but our attempts were frustrated by the energetic particles' rapid erosion of soot during the insertion and removal of the plate.

Consequently, the second explanation remains feasible, with good reasons why the model of Bachelet (2018) and Bachelet et al. (2021), despite being derived to describe the contributions of impacts throughout the flow's depth, might describe such contributions less well than the "thin-flow" model. First, the model of Bachelet et al. (2021) uses profiles u_w and T_w that are measured at the channel's wall and may not be representative of those in the flow's interior. In fact, the mean particle velocity measured at the channel wall $\overline{u}_w$ correlates poorly with the mean velocity $\overline{u}$ calculated with Equation 11 (see Figure 7b), while the monotonically increasing profiles $T_w(z)$ differ from the S-shaped profiles that previous authors propose for granular temperature profiles in the flow's interior (Gollin et al., 2017; Hanes & Walton, 2000; Silbert et al., 2001). Second, Bachelet et al. (2021) may suggest an incorrect dependence of the seismic signal on these profiles, with a particularly strong assumption being that of a frequency-independent attenuation constant γ. We were unable to dramatically improve the predictions of Bachelet et al.'s (2021) model by modifying its inputs, for example, by multiplying the profiles $u_w(z)$ and $\sqrt{T_w(z)}$ by $\overline{u}\ /\ \overline{u}_w$, but, under a different model for the contributions of impacts throughout the flow, such contributions could explain the relationship observed between the mean velocity $\overline{u}$ and the basal force's power spectrum P_F.

To test which explanation accounts for the success of the "thin-flow" model, we suggest that our experimental conditions be replicated with discrete element simulations. In such simulations, a suitably roughened base could be fixed in position to prevent any vibration-induced reduction of its effective friction coefficient and any basal slip, as records of base-adjacent particles' velocities could verify. If the "thin-flow" model continued to be accurate, then the first, "basal slip" explanation would be disproven. Records of particle velocities throughout the flow would then permit variants of Bachelet et al.'s model to be tested and their assumptions examined, using base-normal profiles of velocity and granular temperature measured within the flow's bulk rather than at its edge, to explain and improve on the "thin-flow" model's accuracy. If the "thin-flow" model were no longer accurate, however, then our first explanation would be proven and the model shown to apply only to flows with basal slip. The recorded particle velocities would then permit development of a different model, by which a small number of flow parameters could predict the seismic signal generated by flows without basal slip, analogous to the use of $\overline{u}$ in the "thin-flow" model, or of the inertial number to predict a dense granular flow's kinematic properties.

4.2. The Inertial Number and the Seismic Signal

For given grains, the argument of, for example, da Cruz et al. (2005), that all local, non-dimensional flow parameters should be functions of the local inertial number I, applies as much to the fluctuating forces exerted by a flow as to the flow's kinematic properties. This "$\mu(I)$" framework will not apply where a) the flow's rheology is "non-local", in the sense that the internal stress depends on derivatives of the strain rate rather than on only the strain rate's local value (Clark & Dijksman, 2020), or b) particles are sufficiently agitated that kinetic theory describes their motion better than a mean shear rate (Goldhirsch, 2003), but we can use the framework to discuss our results in the context of Hsu et al. (2014)'s and Taylor and Brodsky (2017)'s.

If the "$\mu(I)$" framework applies within a two-dimensional, steady, fully developed shear flow above a plate with incline $\tan\theta$, a macroscopic force balance implies that I is constant and can be estimated from bulk measurements of the flow's mean velocity $\overline{u}$, volume fraction ϕ, and depth h (Jop et al., 2005), as

$$\hat{I} = \frac{5\overline{u}d}{2\,h\sqrt{\phi g h \cos\theta}}. \tag{22}$$

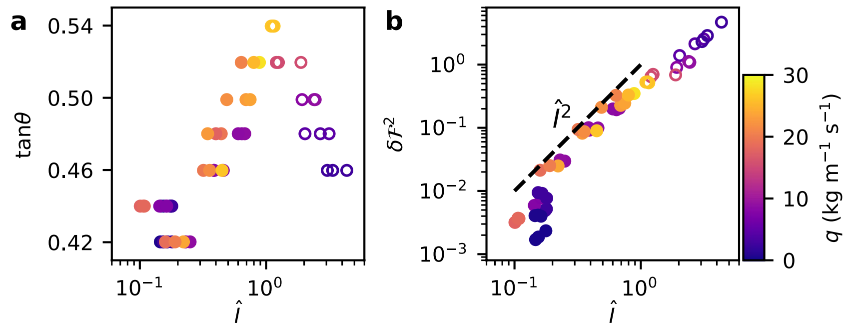

Figure 8. Relations between the inertial number $\hat{I}$ estimated from bulk flow parameters and (a) the channel incline tanθ, (b) the normalized mean squared fluctuating force on the plate $\delta\mathcal{F}^2$. Colors indicate each experiment's mass flux q per unit channel width, and unfilled symbols represent experiments for which the flow was in the transitional regime.

Even if our experimental flows were fully developed, without basal slip, the local inertial numbers within them will have differed significantly from $\hat{I}$. Non-locality will have been particularly significant within slow, thin flows; particles will have been particularly agitated within transitional-regime flows; and friction at the channel's walls will have altered the force balance (Fernández-Nieto et al., 2018). We nevertheless calculated $\hat{I}$ as a descriptor for each flow, with $\phi = \sigma/\rho h$ for flow mass per unit area σ and particle density ρ and with other quantities defined in Sections 2.1 and 2.2. We see in Figure 8a that the "$\mu(I)$" framework applies for the dense experimental flows, insofar as the local, non-dimensional parameter tanθ is closely related to $\hat{I}$.

To examine the relevance to each flow's seismic signal of this inertial number estimate $\hat{I}$, we define a non-dimensional parameter $\delta\mathcal{F}^2$ expressing the mean squared magnitude of high-frequency basal force fluctuations on the instrumented plate, normalied by the mean basal force. From the low-frequency amplitude P_F^0 and corner frequency f_c of the basal force's power spectrum, and from gravitational acceleration g, inclination angle θ, plate length X and width Y, and measured mass overburden σ, we calculate for each flow

$$\delta\mathcal{F}^2 = \frac{2P_F^0 f_c}{(XYg\sigma\cos\theta)^2}. \tag{23}$$

To understand this definition, we recall from Equation 8 that $XYg\sigma\cos\theta$ is the mean normal force applied by the flow to the instrumented plate, over the time interval Δt_c of steady flow recorded by the camera. Meanwhile, as Figure 4 indicates, $2P_F^0 f_c$ approximates the integral of the symmetric power spectral density $P_F(f)$ over all f with $|f| > 1$kHz, this being the lowest frequency accessible to our measurements. Recalling that $\tilde{F}(f)$ is the Fourier transform over Δt_c of the normal force applied to the plate, $P_F(f) = |\tilde{F}(f)|^2/\Delta t_c$. Combining these links and then applying the Plancherel theorem (Plancherel & Mittag-Leffler, 1910) to move to the time domain,

$$2P_F^0 f_c \approx \frac{1}{\Delta t_c}\int_{|f|>1\,\mathrm{kHz}} |\tilde{F}(f)|^2\,\mathrm{d}f = \frac{1}{\Delta t_c}\int_{\Delta t_c} |\delta F(t)|^2\,\mathrm{d}t, \tag{24}$$

where δF is the fluctuating normal force on the plate, high-pass-filtered above 1kHz. Assuming that pressure fluctuations are spatially uncorrelated on the lengthscale of the plate, as discussed in Text S2, $2P_F^0 f_c$ will be proportional to the plate's area XY and $\delta\mathcal{F}^2$ to $1/XY$, but $\delta\mathcal{F}^2$ can be thought of as a rescaling by d^2/XY of a local flow parameter, for mean particle diameter d. Systematic errors in f_c will lead to error in $\delta\mathcal{F}^2$, but this error will be systematic and of negligible magnitude compared to $\delta\mathcal{F}^2$'s range of variation.

Plotting $\delta\mathcal{F}^2$ against $\hat{I}$ for each flow, in Figure 8b, we see that this measure of the high-frequency seismic signal is strongly correlated with the estimated inertial number. This relationship between non-dimensional, local flow parameters is in accord with the "$\mu(I)$" framework, with more energetic flows producing more energetic seismic signals, even for flows to which the "$\mu(I)$" framework is otherwise inapplicable.

Comparing the relation of $\delta\mathcal{F}^2$ and $\hat{I}$ to the relations proposed by previous authors, our results agree more closely with Hsu et al. (2014) than with Taylor and Brodsky (2017). Hsu et al. (2014)'s measurements are

10.1029/2021JF006172

0 not equivalent to ours, but suggest the empirical scaling $\delta\mathcal{F}^2 \sim \hat{I}^{2.0}$, which is a reasonable first approximation to our results and closer than the $\delta\mathcal{F}^2 \sim \hat{I}$ relationship suggested by Taylor and Brodsky (2017)'s observation of direct proportionality between mean squared seismic accelerations and the inertial number. However, it is impossible to make a direct comparison without knowing the frequency-dependence of the Green's function relating the accelerations discussed by Taylor and Brodsky (2017) to the forces imposed by that article's shear flow, while any inconsistency may be due to Taylor and Brodsky (2017)'s different procedure for estimating the inertial number. Differently estimated inertial numbers are likely to be even more inconsistent in geophysical contexts, so any $\delta\mathcal{F}^2\left(\hat{I}\right)$ relation will be harder to apply to geophysical flows than our results in section 3.

4.3. The Application of Our Results to Geophysical Flows

Our results concern the fluctuating forces exerted by laboratory granular flows upon the base on which they travel, so their application to landquake signals necessitates consideration of two things: the Green's function that determines a flow's seismic signal from the forces it exerts, and the differences between geophysical flows' forces and those that we have studied. We limit ourselves to describing the importance of an accurate Green's function, rather than defining one, and to discussing the adjustments involved in moving from laboratory to geophysical flows, rather than validating them, but we nevertheless propose tentative links between our results and the empirical relationships observed by previous authors.

4.3.1. The Importance of an Accurate Green's Function

The forces exerted by a geophysical flow determine a measurable seismic signal only via a Green's function, so an accurate Green's function is necessary to interpret any landquake signal. Even the rate of seismic energy emission, which previous authors have used to describe geophysical flows directly, depends on the response of a flow's base to the forces exerted upon it and hence on the Green's function as well as the flow. This particularly complicates comparisons such as those of Farin et al. (2018), Farin, Mangeney, et al. (2019), and Bachelet et al. (2021), between the seismic energy emitted by geophysical flows and by experimental flows.

Even when different landquake signals are associated with the same Green's function, the signals' relative amplitudes depend on the frequency-dependence of that Green's function, rather than on just the relative magnitudes of the forces exerted by the corresponding flows. Consequently, Green's functions should be considered when assessing landslides' relative magnitudes from their signals' relative amplitudes, as in Norris (1994). We illustrate the Green's function's effect on seismic energy emission and signals' relative magnitudes, using our experimental data, in Text S10.

Calculation of Green's functions will be significantly more difficult for geophysical flows than for our laboratory-scale flows, especially since such functions will vary over time, as a flow propagates downslope, and over a flow's spatial extent at any given time, as the forces exerted by different regions of the flow contribute differently to the signal at a given receiver. However, Allstadt et al. (2020) demonstrates that empirical Green's functions can be used to successfully infer the forces exerted by flows from the seismic signals they generate, and shows that a debris flow's unsaturated, coarse-grained front exerts rapidly fluctuating forces of much greater amplitude than those exerted by its fine-grained, saturated tail. This agrees with previous predictions (Farin, Tsai, et al., 2019; Lai et al., 2018) and suggests that, in the far field, the coarse-grained front's contribution will dominate the seismic signal.

4.3.2. Adjustments to Forces for Geophysical Flows

That debris flows' coarse-grained fronts are so significant in landquake generation indicates the applicability of our results to such flows, as well as to entirely dry rockslides and avalanches, whenever a granular flow's conditions match those of our dense and partially dense experimental flows. The circumstances under which this is true require investigation, but we believe broad applicability to be feasible. This is true whether or not our flows exhibit the vibration-induced basal slip discussed in Section 4.1, since geophysical flows will experience basal slip whenever the friction coefficient of their base falls below its incline, and vibration-induced frictional weakening has been proposed as an explanation for geophysical flows' long runouts (Davies, 1982; Lucas et al., 2014). However, the application of our results to geophysical flows involves significant adjustments, first to the sizes of the flow and its constituent particles and second to the flow's evolution.

Clearly, geophysical flows of interest will be more extensive than our experimental flows and will involve larger particles, but these changes will not alter the underlying physics and simply necessitate adjustment of the values of flow area A and particle diameter d in the models of Section 2.3. According to these models, a flow identical to those in our experiments, except with particles of radius 1 m, should produce a seismic force signal with power spectral density per unit flow area $\hat{P}_F(f)\ /\ A$, of order $(10^2\text{–}10^6)\,\mathrm{N}^2\ \mathrm{m}^{-2}\,\mathrm{s}$ below a corner frequency f_c of order 100 Hz. A more difficult adjustment is required to account for the wide particle polydispersity typical of geophysical flows (Nishiguchi et al., 2012; Takahashi, 1981), which makes d hard to define and necessitates consideration of the segregation of particles by size that is well-documented within granular flows (e.g., Garve, 1925; Gray, 2018). Farin, Tsai, et al. (2019) proposes a promising approach for each given model, of dividing the flow into a coarse-grained front and a fine-grained tail and calculating for each a percentile of the particle size distribution that will be representative, but this proposal requires validation.

Other necessary changes relate to the flow evolution, stemming from differences in particles' coefficient of restitution and in the mechanism of their release. The glass beads in our experiments underwent collisions more elastic than are typical in geophysical flows (Kim et al., 2015), resulting in our observations of sustained saltation at relatively low channel inclinations. This implies that the intense precursory saltation of flow stage I, discussed in Section 3.1, is unlikely to be significant for most geophysical flows, though it may be analogous to rock falls at high slope inclinations. Similarly, the energetic, saltating particles observed in the steady stage III of transitional-regime flows are likely to be rare in geophysical flows, though the coexistence of a dense core and a saltating layer is documented in snow avalanches (Pudasaini & Hutter, 2006).

In fact, the entirety of the experimental flows' stage III is atypical of geophysical flows, since particles were released from the experimental reservoir over a long period at a constant flux, whilst the release of geophysical flows is rarely so steady or protracted. Therefore, our results should only apply to individual stages and regions of an unsteady and spatially varying geophysical flow, over each of which mean flow properties will be representative and related to the local forces exerted on the flow's base. The very front of a flow will resemble stage II of our experimental flows more than the stage III that we have studied in detail, and determination of quantities that are representative of an entire flow requires further work.

4.3.3. Comparisons With Empirical Results

Nevertheless, we can tentatively link our measurements of experimental flows' forces to the landquake signals of geophysical flows, by assuming the validity both of certain adjustments to those forces and of certain restrictions to the Green's function linking geophysical forces to landquake signals. First, we assume that any precursory saltation of a geophysical flow contributes so insignificantly to the signal as to be negligible and that our results apply to a flow area A whose contribution dominates the high-frequency signal. Second, we suppose that the release mechanism and size distribution of geophysical particles significantly affect the signal only by determining the flow's duration and a representative diameter of its particles. Third, we assume that the signal's Green's function is constant over time and corresponds to transmission along a single wave path, without significant dispersion in time. Finally, we consider the signals only at frequencies lower than any force's power spectrum's corner frequency f_c, but high enough for the stochastic impact framework and hence our results to apply.

Under these assumptions, the landquake signal v_r between times t_r and $t_r + \Delta t$ will only depend significantly on the forces exerted by the landslide between times t_s and $t_s + \Delta t$, for some source-receiver delay $t_r - t_s$. Neglecting non-normal components, these forces will have a power spectral density within the relevant frequency band that is equivalent to those that we have studied and is well-described by the constant prediction $\hat{P}_F^0$ of Farin, Tsai, et al. (2019)'s "thin-flow" model, for flow properties averaged between t_s and $t_s + \Delta t$. Writing $\tilde{G}(f)$ for the relevant frequency-space Green's function and f_0 and f_1 for the minimum and maximum frequencies under consideration, the mean squared amplitude of the signal will be

$$\langle v_{r^2} \rangle_{\Delta t} = \frac{2}{\Delta t}\int_{f_0}^{f_1} \left|\tilde{v}_r(f)\right|^2 \mathrm{d}f \approx 2\hat{P}_F^0 \int_{f_0}^{f_1} \left|\tilde{G}(f)\right|^2 \mathrm{d}f. \tag{25}$$

Given this link, we can compare our results to the empirical relations discussed in Section 1.1. Qualitatively, the landquake signal's envelope will have the same shape as the envelope of the time-retarded geophysical force, as Figure 3 shows to be the case for our experimental forces and acceleration signals. Adjusting these envelopes by excluding the precursory saltation and shortening the artificially prolonged stage of steady flow, our results therefore predict the distinctive "spindle-shaped" signal envelopes associated with geophysical granular flows (Suriñach et al., 2005). Quantitatively, our results suggest that a flow's duration will equal its signal's, as in the empirical observations of Deparis et al. (2008), though our experiments are unlike those of Farin et al. (2018) in that our release mechanism prevents comparison with the observed empirical relationship between potential energy loss and signal duration. Similarly, we cannot follow Farin, Mangeney, et al. (2019) in comparing our results to the observations of Norris (1994), that the flow volume is correlated with the signal amplitude.

However, we can compare our results with other empirical relationships for the signal amplitude. Substituting Equation 19 for $\hat{P}_F^0$ into Equation 25 and assuming both constant particle properties and a constant Green's function, our results suggest that a flow of area A in which the particle volume fraction is ϕ and the mean flow velocity is $\overline{u}$ will generate a signal with mean squared amplitude proportional to $\phi A \overline{u}^3$. Rearranging Equation 22 for flow depth h and noting that the mean flow momentum per unit area $q = \rho\phi h\overline{u}$, for particle density ρ, we recover that

$$q^3 = \frac{25\rho^3\phi^2 d^2 \overline{u}^5}{4\hat{I}^2 g\cos\theta} \text{ and } \overline{u}^3 = \left(\frac{4\hat{I}^2 g q^3 \cos\theta}{25\rho^3\phi^2 d^2}\right)^{3/5}, \tag{26}$$

for bulk inertial number $\hat{I}$, representative particle diameter d, gravitational acceleration g, and slope angle θ. Among flows with constant $\hat{I}$ and ϕ, the resulting landquake signals will therefore have root mean squared amplitude

$$v_{rms} \propto A^{1/2} q^{9/10} \cos^{3/10}\theta. \tag{27}$$

Whilst the assumption of constant $\hat{I}$ is very strong, this quantity is close to those found empirically to be approximately proportional to landquake signal amplitude: the work rate against friction used by Schneider et al. (2010), which will be equal to $\mu A q \cos\theta$ for basal friction coefficient μ, and the total flow momentum used by Hibert et al. (2015), equal to Aq. Holding all else constant, the scalings $A^{1/2}$ and A correspond to spatially separated impacts' signals being perfectly uncorrelated and perfectly correlated, respectively, so Text S2 suggests that $A^{1/2}$ is likely to be a better approximation, while the scalings $q^{9/10}$ and q are unlikely to be distinguishable in the field.

5. Conclusion

In conclusion, our experimental apparatus and data analysis permitted us to study the normal force exerted by a granular flow upon the base over which it travels, by measuring its high-frequency power spectral density and testing a range of existing models that predict this spectral density from the flow's properties. Figure 5 shows the "thin-flow" model of Farin, Tsai, et al. (2019) to best predict the spectral density at frequencies well below its corner frequency and demonstrates that our extension of that model to higher frequencies, using Hertz theory, systematically underestimates the corner frequency by 30%. We have proposed that the success of the "thin-flow" model, despite our experimental flows' thickness compared to their constituent particles, can be explained either by slip at each flow's base or by the contributions to the seismic signal of impacts throughout each flow's depth, and we have discussed the adjustments required to apply our results to the landquake signals generated by the forces of geophysical granular flows. Making such adjustments, under certain restrictive assumptions, the "thin-flow" model's predictions are consistent with the empirical observation that a landquake signal's amplitude is approximately proportional to the momentum per unit area of the flow region that generated it.

Finally, our results are also relevant to two open questions on geophysical granular flows' dynamics: 1) the relation between the mean and fluctuating forces exerted by a flow; and 2) the low values of effective friction inferred for many geophysical flows. On the first question, previous authors have suggested that the typical magnitude of fluctuations is proportional to the magnitude of the mean force (Hsu et al., 2014; McCoy et al., 2013), but we show in Figure 8b that the ratio between the two, $\delta\mathcal{F}$, varies over 2 orders of magnitude between our experimental flows, dependent on a bulk inertial number. On the second, acoustic fluidization is one of many possible explanations suggested for the low effective friction necessary to explain many geophysical flows' long runouts (Davies, 1982; Lucas et al., 2014), but we are not aware of it having been previously demonstrated without the application of external forcing. As Figure 7a illustrates, our measurements of μ show the effective friction taking values on the plate lower than the channel incline tanθ, which is implied to be its approximate off-plate value by both the downslope uniformity of the flow at the sidewalls and the saturation of flow velocity observed at the surface. Since the base's roughness is identical in each location, we believe it possible that this reduced friction is associated with the strong acoustic vibrations of the plate, induced by the flow itself.

Conflict of Interest

The authors declare no conflicts of interest relevant to this study.

Data Availability Statement

Experimental data are available at the Pangaea repository (Arran et al., 2020), while computations were performed and plots produced with the summary data and code at Zenodo (Arran et al., 2021), using NumPy (Harris et al., 2020), Matplotlib (Hunter, 2007), and pandas (McKinney, 2010).

Acknowledgments
This work was primarily funded by project ERC-CG-2013-PE10-617472 SLIDEQUAKES, with supporting funds from La Société des Amis de l'ESPCI and from IPGP. We are grateful to Abdelhak Souilah for his construction of the experimental apparatus and to Kate Allstadt, Florent Gimbert, and two anonymous reviewers for their detailed and constructive comments on the manuscript.

References

Allstadt, K. E., Farin, M., Iverson, R. M., Obryk, M. K., Kean, J. W., Tsai, V. C., et al. (2020). Measuring basal force fluctuations of debris flows using seismic recordings and empirical green's functions. *Journal of Geophysical Research: Earth Surface*, *125*(9), e2020JF005590. https://doi.org/10.1029/2020JF005590

Allstadt, K. E., Matoza, R. S., Lockhart, A. B., Moran, S. C., Caplan-Auerbach, J., Haney, M. M., et al. (2018). Seismic and acoustic signatures of surficial mass movements at volcanoes. *Journal of Volcanology and Geothermal Research*, *364*, 76–106. https://doi.org/10.1016/j.jvolgeores.2018.09.007

Arran, M. I., Mangeney, A., de Rosny, J., Farin, M., Toussaint, R., & Roche, O. (2020). *IPGP laboratory data on granular flows' high-frequency seismic signals [data set]*. PANGAEA. https://doi.org/10.1594/PANGAEA.924870

Arran, M. I., Mangeney, A., de Rosny, J., Farin, M., Toussaint, R., & Roche, O. (2021). *Laboratory landquakes, v1.0*. Zenodo. https://doi.org/10.5281/zenodo.4044233

Bachelet, V. (2018). *Étude expérimentale des émissions acoustiques générées par les écoulements granulaires* (Doctoral dissertation, Institut de Physique du Globe de Paris). Retrieved from https://hal.archives-ouvertes.fr/tel-03104582

Bachelet, V., Mangeney, A., Toussaint, R., DeRosny, J., Farin, M., & Hibert, C. (2021). Acoustic emissions of nearly steady and uniform granular flows: A proxy for flow dynamics and velocity fluctuations. *Journal of Geophysical Research: Earth Surface*. Retrieved from https://arxiv.org/pdf/2101.04161.pdf

Börzsönyi, T., & Ecke, R. E. (2006). Rapid granular flows on a rough incline: Phase diagram, gas transition, and effects of air drag. *Physical Review E - Statistical Physics, Plasmas, Fluids, and Related Interdisciplinary Topics*, *74*(6 Pt 1), 061301. https://doi.org/10.1103/physreve.74.061301

Capozza, R., Vanossi, A., Vezzani, A., & Zapperi, S. (2009). Suppression of friction by mechanical vibrations. *Physical Review Letters*, *103*, 085502. https://doi.org/10.1103/PhysRevLett.103.085502

Clark, A. H., & Dijksman, J. A. (2020). Editorial: Non-local modeling and diverging lengthscales in structured fluids. *Frontiers in Physiology*, *8*, 18. https://doi.org/10.3389/fphy.2020.00018

Cuomo, S. (2020). Modelling of flowslides and debris avalanches in natural and engineered slopes: A review. *Geoenvironmental Disasters*, *7*(1), 1–25. https://doi.org/10.1186/s40677-019-0133-9

Dahlen, F. A. (1993). Single-force representation of shallow landslide sources. *Bulletin of the Seismological Society of America*, *83*(1), 130.

Dammeier, F., Moore, J. R., Hammer, C., Haslinger, F., & Loew, S. (2016). Automatic detection of alpine rockslides in continuous seismic data using hidden Markov models. *Journal of Geophysical Research: Earth Surface*, *121*(2), 351–371. https://doi.org/10.1002/2015jf003647

Dammeier, F., Moore, J. R., Haslinger, F., & Loew, S. (2011). Characterization of alpine rockslides using statistical analysis of seismic signals. *Journal of Geophysical Research*, *116*, F04024. https://doi.org/10.1029/2011JF002037

Davies, T. R. H. (1982). Spreading of rock avalanche debris by mechanical fluidization. *Rock Mechanics*, *15*, 9–24. https://doi.org/10.1007/bf01239474

Delannay, R., Valance, A., Mangeney, A., Roche, O., & Richard, P. (2017). Granular and particle-laden flows: From laboratory experiments to field observations. *Journal of Physics D: Applied Physics*, *50*(5), 053001. https://doi.org/10.1088/1361-6463/50/5/053001

Deparis, J., Jongmans, D., Cotton, F., Baillet, L., Thouvenot, F., & Hantz, D. (2008, 08). Analysis of rock-fall and rock-fall avalanche seismograms in the French Alps. *Bulletin of the Seismological Society of America*, *98*(4), 1781–1796. https://doi.org/10.1785/0120070082

Dijksman, J. A., Wortel, G. H., van Dellen, L. T. H., Dauchot, O., & van Hecke, M. (2011). Jamming, yielding, and rheology of weakly vibrated granular media. *Physical Review Letters*, *107*, 108303. https://doi.org/10.1103/PhysRevLett.107.108303

Emam, S., Prochnow, M., Roux, J.-N., & Chevoir, F. (2005). Rheophysics of dense granular materials: Discrete simulation of plane shear flows. *Physical Review E*, *72*, 021309. https://doi.org/10.1103/PhysRevE.72.021309

Farin, M., Mangeney, A., de Rosny, J., Toussaint, R., & Trinh, P.-T. (2018). Link between the dynamics of granular flows and the generated seismic signal: Insights from laboratory experiments. *Journal of Geophysical Research: Earth Surface*, *123*(6), 1407–1429. https://doi.org/10.1029/2017JF004296

Farin, M., Mangeney, A., de Rosny, J., Toussaint, R., & Trinh, P. T. (2019). Relations between the characteristics of granular column collapses and resultant high-frequency seismic signals. *Journal of Geophysical Research: Earth Surface*, *124*(12), 2987–3021. https://doi.org/10.1029/2019JF005258

Farin, M., Tsai, V. C., Lamb, M. P., & Allstadt, K. E. (2019). A physical model of the high-frequency seismic signal generated by debris flows. *Earth Surface Processes and Landforms*, *44*(13), 2529–2543. https://doi.org/10.1002/esp.4677

Ferdowsi, B., Griffa, M., Guyer, R. A., Johnson, P. A., & Carmeliet, J. (2014). Effect of boundary vibration on the frictional behavior of a dense sheared granular layer. *Acta Mechanica*, *225*, 2227–2237. https://doi.org/10.1007/s00707-014-1136-y

Fernández-Nieto, E., Garres-Díaz, J., Mangeney, A., & Narbona-Reina, G. (2018). 2D granular flows with the $\mu(i)$ rheology and side walls friction: A well-balanced multilayer discretization. *Journal of Computational Physics*, *356*, 192–219. https://doi.org/10.1016/j.jcp.2017.11.038

Fleming, R., Taylor, F., U, S., & G, S. (1980). *Estimating the costs of landslide damage in the United States*.U.S. Department of the Interior, Geological Survey. Retrieved from https://books.google.fr/books?id=DGnlhwP6h8cC

Froude, M. J., & Petley, D. N. (2018). Global fatal landslide occurrence from 2004 to 2016. *Natural Hazards and Earth System Sciences*, *18*, 2161–2181. https://doi.org/10.5194/nhess-18-2161-2018

Fuchs, F., Lenhardt, W., & Bokelmann, G., & The AlpArray Working Group. (2018). Seismic detection of rockslides at regional scale: Examples from the Eastern Alps and feasibility of kurtosis-based event location. *Earth Surface Dynamics*, *6*, 955–970. https://doi.org/10.5194/esurf-6-955-2018

Fukao, Y. (1995). Single-force representation of earthquakes due to landslides or the collapse of caverns. *Geophysical Journal International*, *122*(1), 243–248. https://doi.org/10.1111/j.1365-246X.1995.tb03551.x

Gardel, E., Sitaridou, E., Facto, K., Keene, E., Hattam, K., Easwar, N., & Menon, N. (2009). Dynamical fluctuations in dense granular flows. *Philosophical Transactions of the Royal Society A*, *367*(1909), 5109–5121. https://doi.org/10.1098/rsta.2009.0189

Garve, T. W. (1925). Segregation in bins. *Journal of the American Ceramic Society*, *8*, 666–670. https://doi.org/10.1111/j.1151-2916.1925.tb17943.x

Gimbert, F., Fuller, B. M., Lamb, M. P., Tsai, V. C., & Johnson, J. P. L. (2019). Particle transport mechanics and induced seismic noise in steep flume experiments with accelerometer-embedded tracers. *Earth Surface Processes and Landforms*, *44*(1), 219–241. https://doi.org/10.1002/esp.4495

Gimbert, F., & Tsai, V. C. (2015). Predicting short-period, wind-wave-generated seismic noise in coastal regions. *Earth and Planetary Science Letters*, *426*, 280–292. https://doi.org/10.1016/j.epsl.2015.06.017

Given, D. D., Allen, R. M., Baltay, A. S., Bodin, P., Cochran, E. S., Creager, K., et al. (2018). *Revised technical implementation plan for the shakealert system – An earthquake early warning system for the west coast of the United States* (Tech. Rep.). U.S. Geological Survey Open-File Report. https://doi.org/10.3133/ofr20181155

Goldhirsch, I. (2003). Rapid granular flows. *Annual Review of Fluid Mechanics*, *35*(1), 267–293. https://doi.org/10.1146/annurev.fluid.35.101101.161114

Gollin, D., Berzi, D., & Bowman, E. (2017). Extended kinetic theory applied to inclined granular flows: Role of boundaries. *Granular Matter*, *19*, 56. https://doi.org/10.1007/s10035-017-0738-1

Gray, J. M. N. T. (2018). Particle segregation in dense granular flows. *Annual Review of Fluid Mechanics*, *50*(1), 407–433. https://doi.org/10.1146/annurev-fluid-122316-045201

Guzzetti, F., Gariano, S. L., Peruccacci, S., Brunetti, M. T., Marchesini, I., Rossi, M., & Melillo, M. (2020). Geographical landslide early warning systems. *Earth-Science Reviews*, *200*, 102973. https://doi.org/10.1016/j.earscirev.2019.102973

Hanes, D. M., & Walton, O. R. (2000). Simulations and physical measurements of glass spheres flowing down a bumpy incline. *Powder Technology*, *109*(1), 133–144. https://doi.org/10.1016/S0032-5910(99)00232-6

Harris, C. R., Millman, K. J., van der Walt, S. J., Gommers, R., Virtanen, P., Cournapeau, D., et al. (2020). Array programming with NumPy. *Nature*, *585*(7825), 357–362. https://doi.org/10.1038/s41586-020-2649-2

Hertz, H. R. (1881). Uber die Berührung fester elastischer Körper. *Journal für die reine und angewandte Mathematik*, *92*, 156–171.

Hervás, J. E. (2003). *Lessons learnt from landslide disasters in Europe*. *eur 20558 en* (Tech. Rep.). Ispra, Italy: European Commission.

Hibert, C., Ekström, G., & Stark, C. P. (2017). The relationship between bulk-mass momentum and short-period seismic radiation in catastrophic landslides. *Journal of Geophysical Research: Earth Surface*, *122*(5), 1201–1215. https://doi.org/10.1002/2016JF004027

Hibert, C., Mangeney, A., Grandjean, G., Baillard, C., Rivet, D., Shapiro, N. M., et al. (2014). Automated identification, location, and volume estimation of rockfalls at Piton de la Fournaise volcano. *Journal of Geophysical Research: Earth Surface*, *119*(5), 1082–1105. https://doi.org/10.1002/2013JF002970

Hibert, C., Mangeney, A., Grandjean, G., & Shapiro, N. M. (2011). Slope instabilities in Dolomieu crater, Réunion Island: From seismic signals to rockfall characteristics. *Journal of Geophysical Research*, *116*, F04032. https://doi.org/10.1029/2011JF002038

Hibert, C., Stark, C. P., & Ekström, G. (2015). Dynamics of the Oso-steelhead landslide from broadband seismic analysis. *Natural Hazards and Earth System Sciences*, *15*(6), 1265–1273. https://doi.org/10.5194/nhess-15-1265-2015

Hsu, L., Dietrich, W. E., & Sklar, L. S. (2014). Mean and fluctuating basal forces generated by granular flows: Laboratory observations in a large vertically rotating drum. *Journal of Geophysical Research: Earth Surface*, *119*(6), 1283–1309. https://doi.org/10.1002/2013JF003078

Hungr, O., & Morgenstern, N. R. (1984). Experiments on the flow behaviour of granular materials at high velocity in an open channel. *Géotechnique*, *34*(3), 405–413. https://doi.org/10.1680/geot.1984.34.3.405

Hunter, J. D. (2007). Matplotlib: A 2d graphics environment. *Computing in Science & Engineering*, *9*(3), 90–95. https://doi.org/10.1109/MCSE.2007.55

Jing, L., Kwok, C. Y., Leung, Y. F., & Sobral, Y. D. (2016). Characterization of base roughness for granular chute flows. *Physical Review E - Statistical Physics, Plasmas, Fluids, and Related Interdisciplinary Topics*, *94*, 052901. https://doi.org/10.1103/PhysRevE.94.052901

John Steel. (2019). *Fiche technique acier s355*(Tech. Rep.). Retrieved from https://www.john-steel.com/fr/acier/29-plaque-d-acier-decape-et-graisse.html

Johnson, P. A., Savage, H., Knuth, M., Gomberg, J., & Marone, C. (2008). Effects of acoustic waves on stick-slip in granular media and implications for earthquakes. *Nature*, *451*, 57–60. https://doi.org/10.1038/nature06440

Jop, P., Forterre, Y., & Pouliquen, O. (2005). Crucial role of sidewalls in granular surface flows: Consequences for the rheology. *Journal of Fluid Mechanics*, *541*, 167–192. https://doi.org/10.1017/S0022112005005987

Jop, P., Forterre, Y., & Pouliquen, O. (2006). A constitutive law for dense granular flows. *Nature*, *441*(7094), 727–730. https://doi.org/10.1038/nature04801

Kanamori, H., & Given, J. W. (1982). Analysis of long-period seismic waves excited by the May 18, 1980, eruption of Mount St. Helens – A terrestrial monopole? *Journal of Geophysical Research*, *87*(B7), 5422–5432. https://doi.org/10.1029/JB087iB07p05422

Kawakatsu, H. (1989). Centroid single force inversion of seismic waves generated by landslides. *Journal of Geophysical Research*, *94*(B9), 12363–12374. https://doi.org/10.1029/JB094iB09p12363

Kean, J. W., Coe, J. A., Coviello, V., Smith, J. B., McCoy, S. W., & Arattano, M. (2015). Estimating rates of debris flow entrainment from ground vibrations. *Geophysical Research Letters*, *42*(15), 6365–6372. https://doi.org/10.1002/2015GL064811

Kim, D. H., Gratchev, I., Berends, J., & Balasubramaniam, A. (2015). Calibration of restitution coefficients using rockfall simulations based on 3D photogrammetry model: A case study. *Natural Hazards*, *78*, 1931–1946. https://doi.org/10.1007/s11069-015-1811-x

Lai, V. H., Tsai, V. C., Lamb, M. P., Ulizio, T. P., & Beer, A. R. (2018, 06). The seismic signature of debris flows: Flow mechanics and early warning at Montecito, California. *Geophysical Research Letters*, *45*(11), 5528–5535. https://doi.org/10.1029/2018GL077683

Lamb, H. (1904). On the propagation of tremors over the surface of an elastic solid. *Philosophical Transactions of the Royal Society of London A: Mathematical, Physical and Engineering Sciences*, *203*(359–371), 1–42. https://doi.org/10.1098/rsta.1904.0013

Lastakowski, H., Géminard, J.-C., & Vidal, V. (2015). Granular friction: Triggering large events with small vibrations. *Scientific Reports*, *5*, 13455.

Lee, E.-J., Liao, W.-Y., Lin, G.-W., Chen, P., Mu, D., & Lin, C.-W. (2019). Towards automated real-time detection and location of large-scale landslides through seismic waveform back projection. *Geofluids*, *2019*, 1–14. https://doi.org/10.1155/2019/1426019

Lemrich, L., Carmeliet, J., Johnson, P. A., Guyer, R., & Jia, X. (2017). Dynamic induced softening in frictional granular materials investigated by discrete-element-method simulation. *Physical Review E - Statistical Physics, Plasmas, Fluids, and Related Interdisciplinary Topics*, *96*, 062901. https://doi.org/10.1103/PhysRevE.96.062901

Levy, C., Mangeney, A., Bonilla, F., Hibert, C., Calder, E. S., & Smith, P. J. (2015). Friction weakening in granular flows deduced from seismic records at the Soufrière Hills Volcano, Montserrat. *Journal of Geophysical Research: Solid Earth*, *120*(11), 7536–7557. https://doi.org/10.1002/2015JB012151

Léopoldès, J., Jia, X., Tourin, A., & Mangeney, A. (2020). Triggering granular avalanches with ultrasound. *Physical Review E - Statistical Physics, Plasmas, Fluids, and Related Interdisciplinary Topics*, *102*, 042901. https://doi.org/10.1103/PhysRevE.102.042901

Love, A. E. H., & Darwin, G. H. (1888). XVI. The small free vibrations and deformation of a thin elastic shell. *Philosophical Transactions of the Royal Society A*, *179*, 491–546. https://doi.org/10.1098/rsta.1888.0016

Lucas, A., Mangeney, A., & Ampuero, J. P. (2014). Frictional velocity-weakening in landslides on Earth and on other planetary bodies. *Nature Communications*, *5*, 3417. https://doi.org/10.1038/ncomms4417

McCoy, S. W., Tucker, G. E., Kean, J. W., & Coe, J. A. (2013). Field measurement of basal forces generated by erosive debris flows. *Journal of Geophysical Research: Earth Surface*, *118*(2), 589–602. https://doi.org/10.1002/jgrf.20041

McKinney, W. (2010). Data structures for statistical computing in Python. In S. van der Walt & J. Millman (Eds.), *Proceedings of the 9th Python in Science Conference* (pp. 56–61). https://doi.org/10.25080/Majora-92bf1922-00a

MiDi, G. D. R. (2004). On dense granular flows. *The European Physical Journal E*, *14*(4), 341–365. https://doi.org/10.1140/epje/i2003-10153-0

National Research Council. (1985). *Reducing losses from landsliding in the United States*. The National Academies Press.

Nishiguchi, Y., Uchida, T., Takezawa, N., Ishizuka, T., & Mizuyama, T. (2012). Runout characteristics and grain size distribution of large-scale debris flows triggered by deep catastrophic landslides. *International Journal of Erosion Control Engineering*, *5*(1), 16–26. https://doi.org/10.13101/ijece.5.16

Norris, R. D. (1994). Seismicity of rockfalls and avalanches at three cascade range volcanoes: Implications for seismic detection of hazardous mass movements. *Bulletin of the Seismological Society of America*, *84*(6), 1925.

Plancherel, M., & Leffler, M. (1910). Contribution à l'étude de la représentation d'une fonction arbitraire par des intégrales définies. *Rendiconti del Circolo Matematico di Palermo*, *30*(1), 289–335. https://doi.org/10.1007/bf03014877

Pudasaini, S., & Hutter, K. (2006). *Avalanche dynamics: Dynamics of rapid flows of dense granular avalanches*. Springer.

Roche, O., van den Wildenberg, S., Valance, A., Delannay, R., Mangeney, A., Corna, L., & Latchimy, T. (2021). Experimental assessment of the effective friction at the base of granular chute flows on smooth incline. *Physical Review E*. space and Retrieved from https://journals.aps.org/pre/accepted/c5070RbaXb614a1169c09358bf40c9e995b399252

Schneider, D., Bartelt, P., Caplan-Auerbach, J., Christen, M., Huggel, C., & McArdell, B. W. (2010). Insights into rock-ice avalanche dynamics by combined analysis of seismic recordings and a numerical avalanche model. *Journal of Geophysical Research*, *115*, F04026. https://doi.org/10.1029/2010JF001734

Scholl, H. J., Ballard, S., Carnes, S., Herman, A., & Parker, N. (2017). *Informational challenges in early disaster response: The massive Oso/SR530 landslide 2014 as case in point*. Proceedings of the 50th Hawaii International Conference on System Sciences. https://doi.org/10.24251/hicss.2017.302

Schuster, R. L., & Fleming, R. W. (1986). Economic losses and fatalities due to landslides. *Bulletin of the Association of Engineering Geologists*, *23*(1), 11–28.

Sigmund Lindner. (2018). *Product data sheet*. Retrieved from https://www.sigmund-lindner.com/en/products/glass-beads/dispersing-beads/

Silbert, L. E., Ertaş, D., Grest, G. S., Halsey, T. C., Levine, D., & Plimpton, S. J. (2001). Granular flow down an inclined plane: Bagnold scaling and rheology. *Physical Review E - Statistical Physics, Plasmas, Fluids, and Related Interdisciplinary Topics*, *64*, 051302. https://doi.org/10.1103/PhysRevE.64.051302

Steel, S. S. (2019). *Data table for carbon steel s355mc*(Tech. Rep.). Retrieved from https://www.steelss.com/Carbon-steel/s355mc.html

Suriñach, E., Vilajosana, I., Khazaradze, G., Biescas, B., Furdada, G., & Vilaplana, J. M. (2005). Seismic detection and characterization of landslides and other mass movements. *Natural Hazards and Earth System Sciences*, *5*(6), 791–798. https://doi.org/10.5194/nhess-5-791-2005

Taberlet, N., Richard, P., Jenkins, J. T., & Delannay, R. (2007). Density inversion in rapid granular flows: The supported regime. *The European Physical Journal E*, *22*(1), 17–24. https://doi.org/10.1140/epje/e2007-00010-5

Takahashi, T. (1981). Debris flow. *Annual Review of Fluid Mechanics*, *13*(1), 57–77. https://doi.org/10.1146/annurev.fl.13.010181.000421

Taylor, S., & Brodsky, E. E. (2017). Granular temperature measured experimentally in a shear flow by acoustic energy. *Physical Review E - Statistical Physics, Plasmas, Fluids, and Related Interdisciplinary Topics*, *96*, 032913. https://doi.org/10.1103/PhysRevE.96.032913

Tsai, V. C., & Atiganyanun, S. (2014). Green's functions for surface waves in a generic velocity structure. *Bulletin of the Seismological Society of America*, *104*(5), 2573–2578. https://doi.org/10.1785/0120140121

Tsai, V. C., Minchew, B., Lamb, M. P., & Ampuero, J.-P. (2012). A physical model for seismic noise generation from sediment transport in rivers. *Geophysical Research Letters*, *39*, L02404. https://doi.org/10.1029/2011GL050255

Tsang, J. M. F., Dalziel, S. B., & Vriend, N. M. (2019). The granular Blasius problem. *Journal of Fluid Mechanics*, *872*, 784–817. https://doi.org/10.1017/jfm.2019.357

van Asch, T., Malet, J., van Beek, L., & Amitrano, D. (2007). Techniques, advances, problems and issues in numerical modelling of landslide hazard. *Bulletin de la Société Géologique de France*, *178*(2), 65–88.

References From the Supporting Information

Akaike, H. (1971). *Determination of the number of factors by an extended maximum likelihood principle* (Tech. Rep.). Institute of Statistical Mathematics.

Akaike, H. (1974). A new look at the statistical model identification. *IEEE Transactions on Automatic Control*, *19*(6), 716–723. https://doi.org/10.1109/tac.1974.1100705

Akaike, H. (1978). On the likelihood of a time series model. *The Statistician*, *27*(3/4), 217–235. https://doi.org/10.2307/2988185

Babic, M. (1997). Average balance equations for granular materials. *International Journal of Engineering Science*, *35*(5), 523–548. https://doi.org/10.1016/S0020-7225(96)00094-8

Ciarlet, P. G. (1997). Linearly elastic plates. In P. G. Ciarlet (Ed.), Mathematical elasticity (27, pp. 3–127). Elsevier. https://doi.org/10.1016/s0168-2024(97)80007-0

Hurvich, C. M., & Tsai, C.-L. (1989). Regression and time series model selection in small samples. *Biometrika*, *76*(2), 297–307. https://doi.org/10.1093/biomet/76.2.297

Kullback, S., & Leibler, R. A. (1951). On information and sufficiency. *The Annals of Mathematical Statistics*, *22*(1), 79–86. https://doi.org/10.1214/aoms/1177729694

McLaskey, G. C., & Glaser, S. D. (2010). Hertzian impact: Experimental study of the force pulse and resulting stress waves. *Journal of the Acoustical Society of America*, *128*(3), 1087–1096. https://doi.org/10.1121/1.3466847

Michlmayr, G., & Or, D. (2014). Mechanisms for acoustic emissions generation during granular shearing. *Granular Matter*, *16*(5), 627–640. https://doi.org/10.1007/s10035-014-0516-2

Miller, G. F., & Pursey, H. (1954). The field and radiation impedance of mechanical radiators on the free surface of a semi-infinite isotropic solid. *Proceedings of the Royal Society of London A: Mathematical, Physical and Engineering Sciences*, *223*(1155), 521–541. https://doi.org/10.1098/rspa.1954.0134